

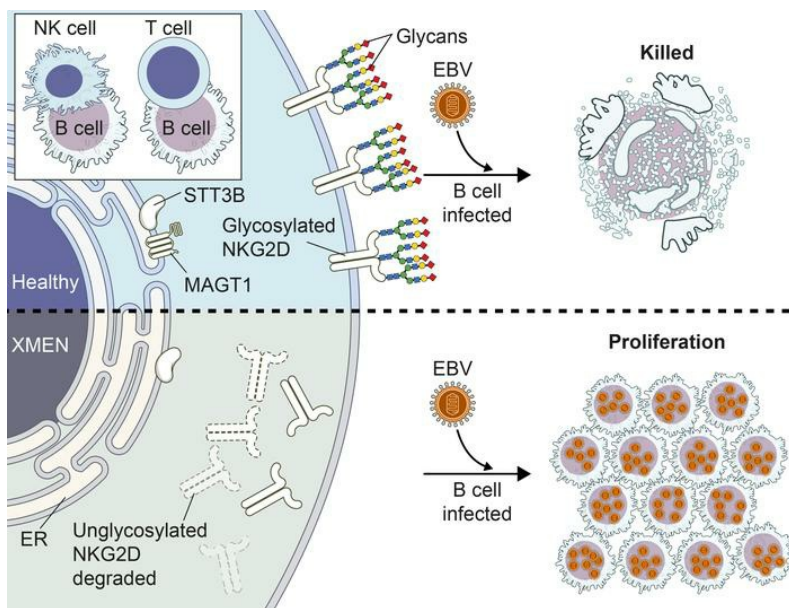
## Defective glycosylation and multisystem abnormalities characterize the primary immunodeficiency XMEN disease

Juan C. Ravell, ... , Matthias Mann, Michael J. Lenardo

*J Clin Invest.* 2019. <https://doi.org/10.1172/JCI131116>.

Research In-Press Preview Immunology

### Graphical abstract



Find the latest version:

<https://jci.me/131116/pdf>



# **Defective glycosylation and multisystem abnormalities characterize the primary immunodeficiency XMEN disease**

Juan C. Ravell<sup>1#</sup>, Mami Matsuda-Lennikov<sup>1,2#</sup>, Samuel D. Chauvin<sup>1</sup>, Juan Zou<sup>1</sup>, Matthew Biancalana<sup>1,3</sup>, Sally J. Deeb<sup>4</sup>, Susan Price<sup>5</sup>, Helen C. Su<sup>5</sup>, Giulia Notarangelo<sup>1, 6</sup>, Ping Jiang<sup>1</sup>, Aaron Morawski<sup>1</sup>, Chrysi Kanellopoulou<sup>1</sup>, Kyle Binder<sup>1,7</sup>, Ratnadeep Mukherjee<sup>8</sup>, James T. Anibal<sup>8</sup>, Brian Sellers<sup>9</sup>, Lixin Zheng<sup>1</sup>, Tingyan He<sup>1,10</sup>, Alex B. George<sup>1</sup>, Stefania Pittaluga<sup>11</sup>, Astin Powers<sup>12</sup>, David E. Kleiner<sup>12</sup>, Devika Kapuria<sup>13</sup>, Marc Ghany<sup>13</sup>, Sally Hunsberger<sup>14</sup>, Jeffrey I. Cohen<sup>15</sup>, Gulbu Uzel<sup>5</sup>, Jenna Bergerson<sup>5</sup>, Lynne Wolfe<sup>16</sup>, Camilo Toro<sup>16</sup>, William Gahl<sup>16</sup>, Les R. Folio<sup>17</sup>, Helen Matthews<sup>1</sup>, Pam Angelus<sup>5,18</sup>, Ivan K. Chinn<sup>19</sup>, Jordan S. Orange<sup>19, 20</sup>, Claudia M. Trujillo-Vargas<sup>21</sup>, Jose Luis Franco<sup>21</sup>, Julio Orrego-Arango<sup>21</sup>, Sebastian Gutiérrez-Hincapié<sup>21</sup>, Niraj Chandrakant Patel<sup>22</sup>, Kimiyo Raymond<sup>23</sup>, Turkan Patiroglu<sup>24</sup>, Ekrem Unal<sup>24</sup>, Musa Karakukcu<sup>24</sup>, Alexandre G. R. Day<sup>25</sup>, Pankaj Mehta<sup>25</sup>, Evan Masutani<sup>1,26</sup>, Suk S. De Ravin<sup>5</sup>, Harry L. Malech<sup>5</sup>, Grégoire Altan-Bonnet<sup>8\*</sup>, V. Koneti Rao<sup>5</sup>, Matthias Mann<sup>4</sup>, and Michael J. Lenardo<sup>1\*</sup>.

<sup>1</sup> Molecular Development of the Immune System Section, Laboratory of Immune System Biology, and Clinical Genomics Program, Division of Intramural Research, National Institute of Allergy and Infectious Diseases (NIAID); <sup>2</sup>Current affiliation: Weizmann Institute of Science, Rehovot, Israel; <sup>3</sup>Current affiliation: New York University Langone Medical Center; <sup>4</sup>Proteomics and Signal Transduction Group and Computational Systems Biochemistry, Max Planck Institute of Biochemistry, D-82152 Martinsried, Germany; <sup>5</sup>Laboratory of Clinical Immunology and Microbiology, Division of Intramural Research, NIAID; <sup>6</sup>Current affiliation: Department of Cell

Biology, Harvard Medical School; <sup>7</sup>Neuroimmunology Branch, National Institute of Neurological Disorders and Stroke; <sup>8</sup>Center for Cancer Research, National Cancer Institute (NCI); <sup>9</sup>Trans-NIH Center for Human Immunology, Autoimmunity, and Inflammation; <sup>10</sup>Department of Rheumatology and Immunology, Shenzhen Children's Hospital, Shenzhen 518038, China; <sup>11</sup>Hematopathology Section, Laboratory of Pathology, NCI; <sup>12</sup>Laboratory of Pathology, NCI; <sup>13</sup>Liver Disease Branch, National Institute of Diabetes and Digestive and Kidney Diseases; <sup>14</sup>Biostatistics Research Branch, NIAID; <sup>15</sup>Medical Virology Section, Laboratory of Infectious Diseases, NIAID; <sup>16</sup>National Human Genome Research Institute; <sup>17</sup>Radiology and Imaging Sciences, Clinical Center, National Institutes of Health; <sup>18</sup>Clinical Monitoring Research Program Directorate, Frederick National Laboratory for Cancer Research, NCI; <sup>19</sup>Texas Children's Hospital, Baylor College of Medicine; <sup>20</sup>Current affiliation: Vagelos College of Physicians and Surgeons, Columbia University; <sup>21</sup>Grupo de Inmunodeficiencias Primarias, Facultad de Medicina, Universidad de Antioquia UdeA, Medellin, Colombia; <sup>22</sup>Department of Pediatrics, Section of Infectious Disease and Immunology, Carolinas Medical Center, Atrium Health - Levine Children's Hospital; <sup>23</sup>Biochemical Genetics Laboratory, Department of Laboratory Medicine and Pathology, Mayo Clinic College of Medicine; <sup>24</sup>Department of Pediatrics, Faculty of Medicine, Erciyes University, Turkey; <sup>25</sup>Department of Physics, Boston University; <sup>26</sup> Current affiliation: University of California San Diego School of Medicine.

#co-first authors

\*co-corresponding authors

The authors have declared that no conflict of interest exists.

## Abstract

X-linked immunodeficiency with magnesium defect, Epstein-Barr virus (EBV) infection, and neoplasia (XMEN) disease is caused by deficiency of the magnesium transporter 1 gene (*MAGT1*). We studied 23 XMEN patients, 8 of whom were EBV-naïve. We observed lymphadenopathy (LAD), cytopenias, liver disease, cavum septum pellucidum, and increased CD4<sup>-</sup>CD8<sup>-</sup>B220<sup>-</sup>TCR $\alpha\beta$ <sup>+</sup> T ( $\alpha\beta$ DNT) cells, in addition to the previously described features of an inverted CD4:CD8 ratio, CD4<sup>+</sup> T lymphocytopenia, increased B cells, dysgammaglobulinemia, and decreased expression of the “Natural-Killer Group 2, member D” (NKG2D) receptor. EBV-associated B cell malignancies occurred frequently in EBV-infected patients. We investigated XMEN patients and autoimmune lymphoproliferative syndrome (ALPS) patients by deep immunophenotyping (32 immune markers) using Time of Flight Mass Cytometry (CyTOF). Our analysis revealed that the abundance of two populations of naïve B cells (CD20<sup>+</sup>CD27<sup>-</sup>CD22<sup>+</sup>IgM<sup>+</sup>HLA-DR<sup>+</sup>CXCR5<sup>+</sup>CXCR4<sup>++</sup>CD10<sup>+</sup>CD38<sup>+</sup> and CD20<sup>+</sup>CD27<sup>-</sup>CD22<sup>+</sup>IgM<sup>+</sup>HLA-DR<sup>+</sup>CXCR5<sup>+</sup>CXCR4<sup>+</sup>CD10<sup>-</sup>CD38<sup>-</sup>) could differentially classify XMEN, ALPS, and normal individuals. We also performed glycoproteomics analysis on T lymphocytes and show that XMEN disease is a congenital disorder of glycosylation that affects a restricted subset of glycoproteins. Transfection of *MAGT1* mRNA enabled us to rescue proteins with defective glycosylation. Together, these data provide new clinical and pathophysiological foundations with important ramifications for the diagnosis and treatment of XMEN disease.

## Introduction

X-linked immunodeficiency with magnesium defect, Epstein-Barr virus (EBV) infection, and neoplasia (XMEN) disease is a rare primary immunodeficiency caused by hemizygous loss-of-function (LOF) mutations in the X-linked magnesium transporter 1 gene (*MAGT1*) in males (1-3). Heterozygous females are healthy carriers with lyonization skewed in their hematopoietic cells to the X chromosome bearing the normal allele(1). *MAGT1* loss was first shown to affect intracellular magnesium ( $Mg^{2+}$ ) homeostasis, leading to defective T cell immune responses and uncontrolled EBV infection with increased susceptibility to EBV<sup>+</sup> lymphoma. Patients had an inverted CD4:CD8 ratio, increased B cells, and decreased surface expression of the activator receptor “Natural-Killer Group 2, member D” (NKG2D) on natural killer (NK) and CD8<sup>+</sup> T cells (1-3). NKG2D loss predisposes to EBV-driven lymphoproliferative disease (LPD) and lymphoma (2, 4). In certain patients, features resembling the autoimmune lymphoproliferative syndrome (ALPS), a disease of lymphocyte homeostasis due to defective FAS-mediated apoptosis, became apparent (5-10). ALPS patients have enlarged secondary lymphoid tissue and an expansion of  $\alpha\beta$  T cells lacking both CD4 and CD8 co-receptors ( $\alpha\beta$ DNT) but expressing the CD45R isoform B220 (11). The full scope of XMEN disease manifestations and their pathogenic cause compared to ALPS has not yet been described.

Protein glycosylation is a post-translational modification critical for normal immune function (12). *MAGT1* has high amino acid sequence homology with the human Tumor Suppressor Candidate 3 protein (TUSC3) and the yeast oligosaccharyl transferase (OST) 3/6 proteins that participate in the enzymatic complex that performs asparagine N-linked glycosylation (NLG) in the endoplasmic reticulum (ER) (13-15). Each OST complex has one catalytic subunit, either STT3A or STT3B, and multiple non-catalytic subunits creating distinct

but complementary NLG enzyme complexes (16, 17). Although there is substantial overlap in the peptides glycosylated by the two OST complexes, STT3A primarily glycosylates substrate peptides co-translationally, whereas STT3B is involved in either co-translational or post-translational glycosylation of peptides skipped by STT3A (17, 18). STT3A preferentially glycosylates acceptor sites in cysteine-rich regions and amino terminus of multipass transmembrane (TM) proteins (19). Conversely, STT3B favors sequons that would be difficult to glycosylate co-translationally, including those in the terminal 50-55 amino acids of the carboxyl tail and short loops between TM regions (18, 19). MAGT1 can associate with the STT3B-containing OST complex and promote the NLG of STT3B-dependent glycoproteins in human tumor cell lines(15, 20). Genetic diseases affecting protein glycosylation, congenital disorders of glycosylation (CDG), can involve genes that add glycans to proteins in the ER (Type-I) or further process protein-bound glycans in the Golgi apparatus (Type-II)(21, 22). The clinical manifestations and severity of CDG are heterogeneous depending on the specific genetic and molecular defects. More recently, a different clinical phenotype manifest by intellectual and developmental disability were described in two patients with *MAGT1* mutations. These individuals had abnormal glycosylation as determined by serum transferrin isoelectric focusing (sTf IEF) and hypoglycosylated STT3B-dependent substrates in patient-derived cell lines (23). However, the extent of the glycosylation defect and an in-depth analysis of the glycopeptides affected by loss of MAGT1 in human lymphocytes have not been described.

In this manuscript, we report new aspects of the largest cohort of EBV-naïve and EBV-infected XMEN patients. We use deep immunophenotyping of peripheral blood mononuclear cells (PBMCs) by mass cytometry combined with a new machine learning algorithm and cluster analysis of multidimensional data to delineate lymphocyte subsets that distinguish XMEN

patients, ALPS patients, and healthy controls. We perform global glycoproteomics analysis of T lymphocytes, which reveals a selective NLG defect in XMEN disease affecting multiple immune proteins. Finally, we show that *MAGT1* mRNA transfection reverses defective glycosylation in peripheral lymphocytes. Together our data show that XMEN disease has previously unidentified features, some of which may be attributable to MAGT1 as a newly recognized facilitator of NLG.

## Results

### Patient Mutations and Demographics

We reviewed the records of 23 patients from 17 unrelated families (A, B, D-R) with LOF *MAGT1* mutations. We observed that XMEN is a multisystem disease more complex than previously appreciated (3, 10, 24-26). (Figure 1A-B, Table 1, and Supplementary Table 1). The cohort was 70% white non-Hispanic, 13% black, 13% multi-race, and 4% Hispanic. All patients were males consistent with X-linked inheritance. Eight individuals (ages 5 – 17 years) were EBV-naïve while fifteen (ages 9 – 50 years) had chronic EBV infection (Supplementary Tables 1 and 2). Two of the EBV-naïve patients subsequently developed EBV infection.

We identified 14 unique molecular alterations of *MAGT1*: missense mutations in 10 families, nucleotide deletions in four, nucleotide insertions in two, and large deletions in two (Supplementary Table 3). The most common mutation (c.409C>T, p.Arg137X) appeared in four unrelated families. The 409 C residue occurs in a CpG dinucleotide, which has a propensity for deamination and conversion of cytosine to thymine, thereby producing the mutation. All mutations tested abolished MAGT1 protein expression (Figure 1C). The most consistent diagnostic finding was decreased NKG2D surface expression on both CD8<sup>+</sup> T cells and NK cells

( $P < 0.0001$ ), making it a hallmark of the disease whether or not EBV infection was present (Figure 1D and Supplementary Figure 1A). Interestingly, we observed that in five families with two male non-identical siblings and no other children, the frequency of coincidence of disease in both males (4/5 families) was much higher than expected by chance ( $P = 0.04$ ).

### **Multisystem abnormalities**

Our examination of this larger cohort of EBV-infected and EBV-naïve patients revealed clinical abnormalities in other organ systems. We observed mild thrombocytopenia (70%) (Figure 2A), transient neutropenia (61%) sometimes associated with mouth sores (Figure 2B), and antibody-mediated cytopenias (35%) (Table 1, and Supplementary Tables 1 and 2). Bone marrow biopsies done to evaluate cytopenias in patients without malignancies showed normal trilineage hematopoiesis. We also found noninfectious liver abnormalities including transient elevations in alanine aminotransferase (ALT) and aspartate aminotransferase (AST) with preserved hepatic function (Figure 2C, Supplementary Table 2). Transient elastography was abnormal in 3 of 7 patients. Liver ultrasound showed increased echogenicity (steatosis) in some patients (Figure 2D). Liver biopsies from both EBV-naïve and EBV-infected patients, and pathology of the liver from a patient who died from EBV-associated lymphoproliferative disease (LPD), revealed variable degrees of periportal inflammatory infiltrates and sinusoidal fibrosis, hepatosteatosis, mild to moderate iron deposits, and diffuse glycogenosis (Figure 2E-G, Supplementary Figure 1I-N, and Supplementary Table 4). All liver specimens from EBV-infected patients were EBV-encoded small RNAs (EBER) negative. Conventional autoantibodies associated with autoimmune hepatitis (AH) were negative, except from one previously reported patient from whom we reviewed the liver biopsy and found no histopathological evidence of AH

(10). Transient and asymptomatic elevations of serum muscle creatine phosphokinase (CPK) were detected (52%). Acute immune-mediated polyneuropathy or Guillain-Barre syndrome (GBS) was seen in one EBV-naïve and three EBV-positive patients. Three patients had seizures. Eight patients had brain imaging (MRI or CT scan) and the most serious finding was atrophy of the cerebrum, cerebellum, brainstem, and spinal cord with calcifications in the basal ganglia and thalami of a 30-year-old male with progressive neurological and cognitive decline (Figure 2H, Supplementary Figure 1G). Two patients ages 45 and 48 had brain atrophy greater than expected for age, and two patients had white matter abnormalities consistent with leukoencephalopathy (Figure 2I). Interestingly, 50% of the patients with brain imaging had cavum septum pellucidum (CSP), a developmental ventricular change of uncertain significance that is found in approximately only 15% of the general population (Figure. 2J). We found no evidence of intellectual disability and/or facial dysmorphism in our XMEN cohort. Taken together, these findings suggest a much broader disease phenotype outside of the immune system than previously suspected.

### **Hypogammaglobulinemia, lymphoproliferation, and malignancy**

Most patients had decreased IgG and IgA with normal IgM associated with recurrent ear and sinus infections (Figure 2K, Table 1 and Supplementary Tables 1 and 2). Upper and lower respiratory infections due to longstanding hypogammaglobulinemia sometimes led to bronchiectasis (Figure 2L). Molluscum contagiosum was seen in 35% of patients (Supplementary Figure 1B). Flat warts affecting predominantly the palms and soles were observed in 30% of the patients, and one young adult developed large perineal condylomata acuminata. These findings suggested a broader immune deficiency than previously noted (1-3).

Many EBV-naïve and EBV-infected patients had chronic LAD (65%) (Figure 3A-D, Supplementary Figure 1C-F, Table 1, and Supplementary Tables 1 and 5). Splenomegaly and lymphoma were detected in half of the patients with persistent EBV viremia while only one EBV-naïve patient had splenomegaly (Figure 3C). A lymph node (LN) biopsy from an EBV-naïve child showed Castleman-like changes (Figure 3E); whereas a tissue biopsy of a large mediastinal mass in another EBV-naïve patient revealed a diffuse, predominantly IgD<sup>+</sup> B lymphoid proliferation without underlying discernible follicular or nodal architecture, and no evidence of clonal expansion (Figure 3F). A LN biopsy from a patient with persistent EBV-viremia revealed florid reactive lymphoid hyperplasia and increased EBER positive cells (Figure 3G). EBV-LPD with a characteristic increase in CD20<sup>+</sup> and CD30<sup>+</sup> cells was observed in a patient with recent EBV-infection (Figure 3H). Lymphoma occurred frequently at a young age in some EBV-infected patients but not in the EBV-naïve patients (Supplementary table 6). The most common neoplasia was Hodgkin lymphoma (HL) (n = 4). A young adult with a history of HL in complete remission (CR) developed EBV-negative liposarcoma (Supplementary Figure 1H).

The immune phenotype of EBV-infected and EBV-naïve XMEN patients was very similar (Supplementary Figure 2, and Supplementary Tables 1 and 2). Characteristic peripheral blood abnormalities included increased B cells (95%) and  $\alpha\beta$ DNT cells (95%). Most patients (78%) had low (<1.1) CD4/CD8 ratios (range 0.17 - 1.9) (Supplementary Figure 2 and Supplementary Table 2). CD4 T cell lymphopenia was noted in 43% of patients, although opportunistic infections were rarely observed. The NK cells and NKT cell counts were normal for most patients. Recent CD31<sup>+</sup> thymic emigrants were also normal (n = 13). The lymphoproliferative disease, lymphoma predisposition and increased DNTs in XMEN disease

were reminiscent of ALPS raising a question as to how these disorders can be distinguished by peripheral blood lymphocyte populations (5-9).

**XMEN patients share some features of ALPS including elevated  $\alpha\beta$ DNTs, defective apoptosis, and secondary lymphoid expansion.**

Most XMEN patients (95%) had elevated  $\alpha\beta$ DNT cells warranting further investigation (Figure 3I, Supplementary Table 2). Because ALPS  $\alpha\beta$ DNTs have been well-documented to express an unusual CD45 glycosylation form similar to mouse B220, we stained PBMCs from healthy controls (HC), ALPS-FAS, and XMEN patients for the CD4 and CD8 co-receptors,  $\alpha\beta$ TCR, and CD45R (B220)(11, 27). By contrast to ALPS, most  $\alpha\beta$ DNT cells from XMEN patients were negative for CD45R (B220) whether the patients were EBV-infected or EBV-naïve (Figure 3I). Notably, XMEN patients did not have marked elevations of the serum biomarkers soluble FasL, IL-10, IL-18, and vitamin B<sub>12</sub>, which can be dramatically elevated in ALPS-FAS (Supplementary Figure 3)(9). We then investigated FAS-induced apoptosis and anti-CD3 restimulation induced cell death (RICD). The latter is a process by which previously activated T lymphocytes undergo clonal depletion upon TCR re-engagement (28). We found that all XMEN patients tested (n = 9) had normal FAS-induced apoptosis but RICD was defective (Figure 3J). By contrast, ALPS cells showed the expected prominent defect in FAS-induced apoptosis and a minor RICD defect (Figure 3J). These data suggest that abnormal RICD may contribute to the expansion of secondary lymphoid tissue in XMEN.

**Leukocyte surface marker clusters distinguish XMEN, ALPS, and healthy controls**

To more precisely define the lymphocyte population differences between XMEN and ALPS patients, we hypothesized that high dimensional phenotyping of PBMCs could reveal novel differences based on surface marker combinations that would not have been previously suspected. If true, this will provide a new and powerful approach for exploring more subtle and complex cellular alterations in immunological diseases that is not possible by conventional flow cytometry analysis. Hence, we stained PBMCs from age-matched XMEN and ALPS patients with a custom-designed antibody panel against 32 surface markers for in-depth immune-phenotyping by Time of Flight Mass Cytometry (CyTOF) (Figure 4, Supplementary Figure 4, Supplementary Table 7). We analyzed PBMCs from 18 XMEN patients, 11 ALPS-FAS patients, and 24 healthy controls (HC), and performed HAL-x (hierarchical agglomerative learning), a new machine learning algorithm to automatically identify clusters of differentiation (CoD) of leukocytes based on distinctive expression levels of surface markers (Figure 4A-C). HAL-x enabled us to execute an unsupervised random forest classification of machine learning attributes with a tunable threshold to self-consistently identify and validate 69 CoD (29, 30). We found that XMEN and ALPS patients had 6 and 2 CoD, respectively, that were statistically significantly different from HC (Supplementary Figure 5). Specifically, XMEN patients had a remarkably subtle distinct immunological signature due to multiple elevated populations of naïve B cells (Figure 4C). We then ranked the CoDs to classify the samples and found that two populations of naïve B cells, CoD #32 (CD20<sup>+</sup>CD27<sup>-</sup>CD22<sup>+</sup>IgM<sup>+</sup>HLA-DR<sup>+</sup>CXCR5<sup>+</sup>CXCR4<sup>++</sup>CD10<sup>+</sup>CD38<sup>+</sup>) and CoD #34 (CD20<sup>+</sup>CD27<sup>-</sup>CD22<sup>+</sup>IgM<sup>+</sup>HLA-DR<sup>+</sup>CXCR5<sup>+</sup>CXCR4<sup>+</sup>CD10<sup>-</sup>CD38<sup>-</sup>), were sufficient to generate receiver operator characteristics that achieved a near-perfect classification of our samples as either XMEN, ALPS or healthy controls (Figure 4D, Supplementary Figure 6A-B). The specific cell markers for statistically different CoD are shown in Supplementary

Figures 6B and 7A-B. To compare and validate the findings from our novel pipeline, we also performed high-dimensional cluster analysis of the CyTOF data using Phenograph (Supplementary Figure 8A-C)(31). Ranking of the Phenograph-generated CoDs (PG-CoDs) revealed one population of naïve B cells, PG-CoD #0 (CD20<sup>+</sup>CD27<sup>-</sup>CD22<sup>+</sup>IgM<sup>+</sup>HLA-DR<sup>+</sup>CCR6<sup>+</sup>CXCR5<sup>+</sup>CXCR4<sup>++</sup>CD10<sup>+</sup>CD38<sup>+</sup>) and one population of cytotoxic T cells, PG-CoD #22 (CD3<sup>+</sup>CD8<sup>+</sup>CD27<sup>+</sup>CD45RA<sup>+</sup>PD-1<sup>+</sup>CD38<sup>+</sup>CD57<sup>+</sup>CD314/NKG2D<sup>+</sup>) as the lymphocyte subsets with the most divergent abundance between HC, XMEN, and ALPS patients (Supplementary Figures 9 and 10A-B). Our Phenograph analysis also showed 7 additional lymphocyte subsets (PG-CoD # 2, 6, 10, 13, 14, 18, and 19) that distinguished XMEN from both HC and ALPS (Supplementary Figures 9 and 11). Thus, the mass cytometry analysis of XMEN and ALPS patients uncovered both global as well as remarkably subtle but characteristic CoD patterns of peripheral blood leukocytes in these diseases.

### **Restricted NLG defect in XMEN patients**

Because of the broader scope of the clinical findings, we sought additional pathogenetic mechanisms besides the alteration of Mg<sup>2+</sup> transport. Our bioinformatics analysis and other data showed that MAGT1 is the human homologue of the yeast OST3/6 subunit of the OST complex and functions in NLG (16, 17, 20, 23). The recently reported structure of the yeast OST complex showed an integral association of two transmembrane helices of OST3 with transmembrane segments of the major catalytic STT3 subunit (32)(Figure 5A). We hypothesized that the selective reduction of NKG2D but not that of other surface proteins such as CD5 in XMEN was due to abnormal glycosylation (Figure 5B). NKG2D is a dimeric single-pass transmembrane glycoprotein of the C-type lectin-like family of receptors (2, 33, 34). It forms a tetrameric

complex with two copies of the signaling protein DAP10 that is obligatory for cell surface expression (Supplementary Figure 12A). Silencing the expression of human NKG2D or DAP10 decreases the cytotoxic effector function of CD8<sup>+</sup> T cells and NK cells (34). Human NKG2D has three predicted asparagine-X-serine/threonine (NXS/T) motif NLG sites, where X is any amino acid except proline: Asn131 and Asn163, which are conserved, and Asn202 which differs in location compared to murine NKG2D (35) (Supplementary Figure 12A). Consistent with previous results, we observed that the full-length NKG2D glycosylated species that is observed as a broad band between 42 and 50 kDa (Figure 5C, lane 1, band 3) in the HC is replaced in XMEN with a smaller less intense band migrating at 25 kDa and several faint indistinct bands ranging up to 28 kDa (Figure 5C, lane 3, band 1), which we hypothesized were partially glycosylated forms in XMEN patient samples. Treatment with N-glycosidase F (PNGase F), which removes almost all N-linked oligosaccharides from glycoproteins, caused these bands to collapse into the presumptive unglycosylated polypeptide of 23 kDa expected for a 216-amino acid protein (Figure 5C, lane 2, band 0). This unglycosylated polypeptide was markedly less abundant in XMEN patient samples presumably due to instability of the partially glycosylated NKG2D protein (Figure 5C, lane 4, band 0). As expected, MAGT1 protein was absent from the patient lysates compared to HC's (Figure 5C, middle panel, lane 3 and 4). These data raised the question of whether defective NLG accounted for decreased surface NKG2D expression. Therefore, we treated T cells from HC with tunicamycin, an inhibitor of NLG, for 24 hours and found that this dramatically reduced NKG2D surface expression but only mildly affected CD5 expression (Figure 5D). Biochemical analysis showed that the fully glycosylated NKG2D species (Figure 5E, lane 1, band 1) and the non-glycosylated polypeptide revealed by PNGase F treatment (Figure 5E, lane 2, band 2) were diminished by tunicamycin treatment (Figure 5E, lane

3, band 1 and lane 4, band 2, respectively). Taken together, these data show that directly impairing glycosylation causes instability and loss of the NKG2D protein thereby reducing cell surface expression. Hence this provides a paradigm of how defective glycosylation could interfere with the proper expression of NKG2D leading to impaired EBV anti-viral immunity.

To further investigate the NLG defect due to the absence of MAGT1, we performed glycoproteomic analysis on T cells from 3 XMEN patients and 3 HC using filter-aided mixed-lectin glycopeptide capture followed by peptide identification by liquid chromatography and dual mass spectrometry (LC-MSMS)(36). In total, sequence data were obtained for 2481 peptides from 1421 proteins, of which essentially all contained the canonical NXS/T sequon (Supplementary Figure 12B-C). Comparing the glycoacceptor sites, we found that the abnormal XMEN subset had a serine/threonine (S/T) ratio of 1.56 whereas the total dataset had a ratio of 0.75 (Supplementary Figure 12B). Hence, proteins perturbed by the loss of MAGT1 predominantly contain the NXS sequon with a smaller fraction containing the NXT sequon consistent with observations in the yeast  $\Delta\text{ost3}\Delta\text{ost6}$  knockout (37, 38). Although the proteins had a broad cellular distribution, over 50% were derived from the endoplasmic reticulum (ER) or the cell membrane (Supplementary Figure 12D). Unsupervised hierarchical clustering of the glycopeptide abundances readily sorted the samples into two distinct groups that corresponded to the MAGT1-deficient XMEN patients and the HC that were not immediately obvious in comparing all peptides (Supplementary Figure 12E). However, with a more refined heat map of the differences, we found 105 specific glycopeptides encoded by 73 unique genes having one or more glycopeptide in the samples from XMEN patients (Figure 5F, Supplemental Excel file 1). Most of the NLG alterations that had a significant  $p$  value in a t-test comparison of XMEN to HC exhibited lower glycosylation though a few had higher glycosylation (Supplementary Figure

12F, red dots, Supplemental Excel file 1). Since the lack of glycoproteins could result from decreased protein abundance, we also examined the complete LC-MS/MS proteome. This did not reveal major peptide abundance differences between the XMEN and HC lysates except for the marked reduction of MAGT1 protein in all the XMEN samples, confirming that the gene mutations in these individuals abrogated protein expression (Supplementary Figure 12G). Because both XMEN and HC displayed incomplete glycosylation, we compared both using a scatter plot of the log (glycosite/protein), which shows that XMEN samples have more peptides with lower glycosylation site occupancy compared to HC supporting the conclusion that MAGT1 deficiency leads to a selective NLG defect (Supplementary Figure 12H, red dots).

More detailed examination of the dataset showed, as expected, that peptides from NKG2D containing the Asn131 and Asn202 residues had reduced glycosylation; no peptide with Asn163 was detected (Supplemental Excel file 1). We also found underglycosylation of other key immune regulatory molecules including the co-stimulatory molecule CD28, CD70 (or Tumor Necrosis Factor (Ligand) Superfamily, Member 7), the major histocompatibility complex protein HLA-DRB1, the T cell receptor  $\alpha$  chain (TCR- $\alpha$ ), the ceramide synthase 2 (CERS2) protein, and the Solute Carrier Family 4 Member 7 (SLC4A7) protein, all of which might contribute to the vulnerability of XMEN patients to EBV and other infectious agents (Figure 6A-B, Supplemental Excel file 1). Notably, the glycoproteomics mass spectrometry detected reduced NLG of the T cell receptor  $\alpha$  chain (TCR- $\alpha$ ), but we also detected defective glycosylation of the T cell receptor  $\beta$  chain (TCR- $\beta$ ) by western blotting. Since CD28, CD70, HLA-DRB1, and TCR- $\beta$  must be expressed on the cell surface to execute their immune function, we used flow cytometry to test whether reduced NLG affected surface expression on T cells from XMEN patients (Figure 6A). CD28, CD70 and HLA-DRB1 showed a marked reduction in surface

expression. Surprisingly, it appeared that TCR- $\beta$  surface immunolabeling on T cells was increased in XMEN. We surmised this was due to less steric interference with the staining antibody binding due to underglycosylation because the level of protein was mildly reduced rather than increased in the XMEN samples by western blot (Figure 6B). We therefore treated T cells from healthy controls with tunicamycin for 48 hours and found that despite a relative decrease in total TCR- $\beta$  expression in the tunicamycin-treated samples as determined by immunoblotting (Supplementary Figure 12I), its surface immunolabeling by flow cytometry appeared to be increased, especially at lower concentrations of tunicamycin consistent with the hypothesis of steric interference with antibody binding by glycosylation (Supplementary Figure 12J).

We also examined other immunologically important molecules. We observed that impaired glycosylation of CD28 in T cells from XMEN patients also correlated with its decreased protein expression by western blot (Figure 6C), and tunicamycin treatment of T cells from healthy controls showed a dose-dependent decrease in expression of both the total and fully glycosylated CD28, and an increase in the presumptive unglycosylated form (Figure 6D). Reduced glycosylation was verified by western blotting for CD28, CD70, HLA-DRB1, TCR- $\beta$ , CERS2, and SLC4A7 proteins for which we saw a reduction in fully or partly glycosylated species (Figure 6B, bands 1 or 2; and Fig. 6C, band 1) to underglycosylated or non-glycosylated species in the XMEN samples compared to the HC (Figure 6B, bands 0 or 1). The high molecular weight species of CD70 and TCR- $\beta$  are likely due to modification of the oligosaccharide core in the Golgi (39). We also assessed surface protein expression and glycosylation status of ICAM-3 by flow cytometry and western blotting, respectively, and confirmed that this protein is representative of over-glycosylated proteins in XMEN disease

(Supplementary Figure 12K-L). Overall, we found that the affected 73 proteins fall into at least 6 categories: neural function, glycosylation, transport, adhesion, immunity, and lipid metabolism with 18 being uncategorized (Figure 6E). A large number of these are associated with disease states affecting different organ systems, especially the hemopoietic system, when they are genetically deficient (Supplementary Table 8). Thus, while most proteins in XMEN cells appeared to be represented equivalently to normal cells, a small select group, affecting a diverse set of cellular processes, show abnormal glycosylation in MAGT1-deficient cells. Certain of these, though not necessarily all, may contribute for the broader phenotype we observe depending on the specific functional effect of the glycosylation defect on the role of the individual protein in its cellular pathway.

Because of the clear glycosylation defects in XMEN patients, we investigated both the carbohydrate deficient transferrin (CDT) test and the apolipoprotein CIII (Apo-CIII) isoforms as clinical adjuvants for the screening of XMEN disease(21). Apo-CIII is a single core 1 mucin type O-glycosylated protein that carries a single O-glycan at Thr-94 and is not N-glycosylated (40). All XMEN patients tested (n=10) had a mild but distinctly abnormal glycosylation pattern on mass spectrometry resembling a CDG Type-I, but displayed a unique combined defect in both CDT and Apo-CIII glycosylation. Most of the transferrin molecules from XMEN patient cells had fully glycosylated asparagine sites (Figure 6F, pattern 3), but some were defective for the initial transfer of the oligosaccharide precursor from the dolichol carrier leaving unoccupied asparagine glycosylation sites (Figure 6F, pattern 1, and Supplementary Table 9). Transferrin from XMEN patient cells also exhibited a mild defect in final processing of oligosaccharides with sialic acid (Figure 6F, pattern 2). The Apo-CIII O-linked glycosylation (OLG) that we observed for some patients could be a secondary effect of defective NLG of enzymes/proteins

important for OLG (Supplementary Table 9). Thus, these tests reveal the nature and extent of the glycosylation defect and provide useful additional clinical diagnostic tools for XMEN disease.

### **Affected N-glycosylation sites are close to transmembrane regions**

To investigate whether the N-glycosylation sites affected in XMEN disease are STT3A or STT3B-dependent, we performed a prediction analysis of our glycoproteomic site occupancy dataset. We found that only 36% and 17% of the differentially glycosylated peptides mapped to STT3B- and STT3A-predicted motifs respectively (Supplemental Excel file 1). Interestingly, we found that the majority (57%) of the affected sequons were within 60 amino acids of a TM region, and these peptides accounted for most (83%) of the STT3A-dependent peptides (Figure 7A, Supplemental Excel file 1). We also observed that most glycosylation sequons that mapped to a described protein region were hypoglycosylated (Figure 7B).

### **Defective glycosylation can be corrected by RNA replacement**

Finally, we explored the hypothesis that restoring *MAGT1* gene expression might reverse the glycosylation defects in XMEN. We transfected synthetic mRNAs encoding *MAGT1* or a GFP control into XMEN patient PBMCs *ex vivo* using the Maxcyte transfection device. This procedure achieved greater than 90% transfection efficiency with high cell viability. At 48-72 hours after transfection, the cells were analyzed by flow cytometry which showed that surface expression of key glycoproteins including NKG2D and CD70 were restored (Figure 8A). We further examined the specific glycosylated protein forms using western blotting. We found that the fully glycosylated forms of NKG2D, CD70, CERS2, SLC4A7 and TCR- $\beta$  proteins were mostly or completely rescued by mRNA transfection-mediated expression of *MAGT1* (Figure 8B).

## Discussion

In a larger group of patients, we found new features that were not manifested or recognized in the earlier cases (1-3). Here we report a comprehensive clinical description of the largest cohort of XMEN patients yet described. We found that XMEN disease is a complex multisystem disorder. Although all patients had *MAGT1* mutations that cause complete protein loss, the disease has variable expressivity, even among individuals harboring the same mutation. Classic XMEN disease can now be recognized as affecting males with recurrent ear and sinopulmonary infections, lymphadenopathy (LAD) with or without splenomegaly, AI cytopenias, and/or LPD (Table 1). Remarkably, EBV-naïve and EBV-infected XMEN are clinically similar except for lymphoma and EBV-LPD, which occur exclusively in the latter. Mild thrombocytopenia, neutropenia, elevated liver enzymes, and increased CPK levels are more variable in occurrence and normal results do not rule out XMEN disease. Other common findings are increased B cells, an inverted CD4:CD8 ratio, elevated  $\alpha\beta$ DNT cells, low serum IgG and IgA, and CD4<sup>+</sup> lymphopenia. Chronic EBV viremia was characteristic of XMEN patients who were EBV-infected, confirming our previous observations (1). The expanded set of clinical features and diagnostic tests should allow clinicians to make a positive presumptive diagnosis that can then be confirmed by molecular testing.

An important new insight that emerged from exploring the molecular details of *MAGT1* as a component of OST complexes involved in NLG was that it controls a specific pattern of glycoproteins that are important for proper immune function. Our mass spectrometry glycoproteomics analysis on T lymphocytes was able to detect a surprisingly small and distinctive set of glycosylation changes between patients and controls. We confirmed that there were 73 unique proteins whose glycosylation was affected and have demonstrated that several of

the hypoglycosylated proteins important for immunity have secondarily decreased expression. However, the MAGT1-dependent glycoproteins are a tiny subset of the thousands of proteins that undergo post-translational NLG.

Our glycoproteomics analysis also revealed that defective glycosylation in XMEN disease preferentially affects NxS sequons. We found most affected glycosites were located within 60 amino acids of TM domains, including both acceptor sites predicted to be STT3A- and STT3B-dependent, which represents a novel class of MAGT1-facilitated sites. We show that MAGT1 deficiency causes a more immune-restricted and less severe clinical presentation than STT3B deficiency or other CDGs, in which brain and neurodevelopmental abnormalities, intellectual disability, failure to thrive, severe liver disease, and hypotonia are commonly seen (21, 22, 41). In contrast to a recent report, we did not find intellectual disability or dysmorphic features in our cohort of patients, including two patients (only one reported here) with the same c.991C>T (p.R331X) *MAGT1* mutation (23). This suggests that loss of MAGT1 expression alone does not lead to intellectual disability. We did observe varying degrees of brain, cerebellar, and/or spinal cord atrophy in three patients. Because cerebellar atrophy has been described in STT3B deficiency, defective glycosylation may play a role in these central nervous system (CNS) findings (42). Liver disease is commonly seen in CDG and intermittent elevations of liver enzymes (AST/ALT) were noted in XMEN. However, liver biopsies did not reveal a specific pattern of injury. Liver disease in EBV-naïve patients shows that EBV is not the cause, so it may relate to impaired glycosylation.

We show that the glycosylation of transferrin as detected by a clinical mass spectrometry assay is clearly abnormal in all XMEN patients tested. Although it was recently reported that MAGT1 deficiency results in a type-1 sTf IEF pattern, we now show that sTf from XMEN

patients also have a mild defect in final processing of the glycans (23). Furthermore, and in contrast with most CDG type-I where Apo-CIII is not affected, XMEN patients may also have an OLG defect in Apo-CIII, which could be secondary to defective NLG of components of the OLG enzymatic apparatus. Nevertheless, the limited but broader range of glycosylation defects we describe compared to our earlier reports may offer a window for further investigation into the expanded phenotype of XMEN patients. We now propose that XMEN is a restricted CDG. The presence of a CDT and Apo-CIII isoform pattern similar to the one observed in this study (Supplementary Table 9) in a male patient with a suspected CDG, should prompt further immune and genetic testing for XMEN disease. Since we know very little about how specific amino acid residues in the MAGT1 protein carry out function, having a simple straightforward clinical diagnostic test is useful. Both staining for NKG2D (which may or may not be available in different hospitals) as well as the CDT test can help solidify the diagnosis.

Interestingly, we found defective glycosylation of certain ion transporters in XMEN samples, and  $Mg^{2+}$  deficiency can affect glycosylation (15). The *MAGT1* gene is conserved in unicellular eukaryotes such as yeast, indicating an ancient phylogenetic connection between glycosylation and  $Mg^{2+}$  (13). Previously, abnormalities of intracellular levels and transport of  $Mg^{2+}$  have been found in XMEN patients (1, 2). However, both total and ionized serum magnesium concentrations are normal and, hence, are not diagnostic of XMEN (Supplementary Table 2). Intracellular  $Mg^{2+}$  determination or TCR-induced  $Mg^{2+}$  fluxes have been extensively tested and not proven useful for clinical diagnostic tests. These assays are based on fluorescent dyes that bind  $Mg^{2+}$  but which also have low affinity for calcium  $Ca^{2+}$  and other ions. Thus, results can be compromised by fluctuations in  $Ca^{2+}$  concentrations and intracellular dye compartmentalization among other variables and are therefore unreliable. The previously

reported NKG2D surface expression deficiency remains the best flow cytometry diagnostic test and this can now be augmented with the CDT test (1, 2).

Another important clinical insight derived from our study is the recognition that XMEN has certain clinical similarities to ALPS and should be considered in the differential diagnosis for the latter disease. LAD, previously attributed to uncontrolled EBV-infection in XMEN, was detected in both EBV-naïve and EBV-infected patients. Interestingly, both ALPS and XMEN disease have apoptotic effects that may contribute to secondary lymphoid expansion, but in ALPS, this primarily involves defective FAS-induced apoptosis, whereas in XMEN it is due to defective RICD. One shared abnormal population are  $\alpha\beta$ DNTs but in ALPS this population characteristically expresses high CD45R (B220) whereas we show that in XMEN it does not. In addition, these two diseases have other distinct clinical features and a genetic difference, all of which will aid proper diagnosis and treatment (Supplementary Table 10). In order to define the differences between these diseases and healthy humans, we undertook deep immunophenotyping with a multidimensional CyTOF procedure yielding 69 different CoD groups. Using a new machine learning pipeline (HAL-x), we defined two rare naïve B cell populations that accurately discriminate between XMEN, ALPS, and healthy controls. We also used a classical high-dimensional clustering method (Phenograph) to validate and expand our CyTOF analyses. It will be of great interest to examine these newly defined cell populations functionally and determine whether and how they contribute to disease pathogenesis.

Finally, we discovered that CD70, whose genetic deficiency was recently shown to predispose to uncontrolled EBV infection and hypogammaglobulinemia, is underglycosylated and has reduced surface expression on XMEN lymphocytes (43). We also now demonstrate that reduced surface expression of NKG2D occurs when glycosylation is abrogated. Therefore, there

are two key molecules whose restoration by improved glycosylation may enhance anti-viral immunity against EBV, which is a strongly lymphotropic and oncogenic virus. We also show that mRNA transfection can achieve restoration of these and other glycoproteins. This provides evidence that gene transfer approaches to restoration of MAGT1 expression in patients with XMEN disease might rescue critical cellular functions. However, restoration of MAGT1 in blood cells may not be sufficient to correct abnormalities in all organ systems.

## **Methods**

### **Patients**

Twenty XMEN patients were seen at the National Institute of Allergy and Infectious Diseases (NIAID) and three elsewhere with samples evaluated at the National Institutes of Health (NIH).

### **Cells**

PBMCs were isolated by Ficoll-Paque PLUS (GE Healthcare) gradient density centrifugation and ACK lysis (Quality Biological). PBMCs were cryopreserved in liquid nitrogen in dialyzed fetal bovine serum (FBS) containing 10% dimethyl sulfoxide (DMSO).

### **Activation and expansion of human T lymphocytes**

Cryopreserved PBMCs were rapidly thawed and washed in pre-warmed complete RPMI-1640 medium (Lonza) containing 10% FBS, 2 mM glutamine, and penicillin and streptomycin (100 U/mL each, Invitrogen). Cells at  $1 \times 10^6$ /mL were stimulated with anti-CD3 (HIT3a, Biolegend) and anti-CD28 (CD28.8, Biolegend) at 1  $\mu$ g/mL each in complete RPMI medium.

After 3 days, cells were supplemented with 100 U/mL of recombinant human Interleukin-2 (rhIL-2, R&D).

### **Tunicamycin treatment**

Tunicamycin (Sigma-Aldrich) was dissolved in DMSO to generate a concentrated stock solution. T cells from healthy donors were activated and cultured for 7-14 days prior to tunicamycin treatment. Cells ( $1 \times 10^6$  to  $1 \times 10^7$ ) were treated with 10  $\mu\text{g/mL}$  tunicamycin or DMSO as vehicle control at a cell density of  $5 \times 10^5$  cells/mL in complete RPMI-1640 medium containing 10% FBS, 2 mM glutamine, penicillin and streptomycin (100 U/mL each, Invitrogen), and 100 U/mL of recombinant human Interleukin-2 (rhIL-2, R&D) for the specified time at 37°C in a 5% CO<sub>2</sub> ambient. Lower tunicamycin concentrations at 1 and 3  $\mu\text{g/mL}$  were also used for the determination of TCR- $\beta$  surface expression by flow cytometry experiment.

### **Deglycosylation**

$5 \times 10^6$  cells were lysed in 100  $\mu\text{l}$  of RIPA lysis buffer (1% NP-40, 150mM NaCl, 50mM Tris-HCl (pH 7.4)) with protease inhibitor (Roche). The lysates were then centrifuged at 14,000 rpm at 4 °C for 10 minutes to remove insoluble material and treated with PNGase F (New England BioLabs) according to the manufacturer instruction. Briefly, a stock of 10x denaturation buffer (5% SDS and 400 mM DTT) was added to the samples to a final concentration of 1x. The samples were denatured at 100°C for 10 minutes and then chilled on ice. Denatured samples were mixed with 2  $\mu\text{l}$  of 10X Glyco Buffer 2 and 2  $\mu\text{l}$  of 10% NP-40, then diluted to 20  $\mu\text{l}$  with water. 20  $\mu\text{l}$  of the mixture were then transferred to 2 separate tubes (i.e. 40  $\mu\text{l}$  total). One tube

was treated with 1  $\mu$ l of PNGase F (500,000 units/mL, New England BioLabs Inc) and the other with ddH<sub>2</sub>O vehicle at 37 °C for 1hour.

### **FAS-receptor mediated apoptosis (FAS-kill assay) and Restimulation induced cell death (RICD) assays**

Cultured T-lymphocytes were washed and re-suspended in RPMI without IL-2. Cells ( $1 \times 10^5$  cells/0.2 mL media/well) were plated in triplicates in 96-well round bottom plates and treated with varying concentrations of agonistic anti-FAS antibody (APO-1-3, Enzo Life Sciences) plus Protein A (Sigma-Aldrich) at twice the concentration of the anti-FAS antibody or anti-human CD3 antibody (HIT3a, Biolegend) for 24 hours. Nonviable cells were stained with 5  $\mu$ g/mL propidium iodine (Sigma-Aldrich). Cell death was quantified by flow cytometry using an LSR II (BD Biosciences), analyzed in FlowJo (Tree Star) and plotted in Prism (GraphPad).

### **Plasma biomarkers**

Plasma biomarkers were quantified with Quantikine kits (R&D Systems) following the manufacturer's instructions (44). A mixed effect statistical model with a likelihood ratio test was used to analyze the data using R version 3.3.2(45).

### **Flow cytometry**

Cryopreserved PBMCs were thawed and incubated with human Fc receptor blocking solution (Biolegend) and Zombie Green viability dye (Biolegend) in PBS at 25°C for 20 minutes. Cells were stained in ice-cold FACS buffer (Dulbecco's Phosphate-Buffered Saline, 2% FCS, and 1% sodium azide) with fluorochrome-conjugated antibodies on ice for 30 minutes. T cell

blasts were processed similarly but without incubation with human Fc receptor blocker and viability dye. The following antibodies were used: anti-CD3 (UCHT1, Invitrogen; HIT3a or SK7), CD4 (OKT4 or RPA-T4), CD5 (L17F12), CD8 (RPA-T8 or SK1), CD16 (3G8), CD20 (2H7), CD45R/B220 (RA-3-6B2) or rat IgG2 $\alpha$ k isotype control (RTK2758), CD28 (CD28.2), CD50/ICAM-3 (CBR-IC3/1), CD56 (MEM-188), CD70 (113-16), CD314/NKG2D (1D11) or mouse IgG1 $\kappa$  isotype control (MOPC-21), HLA-DR (Tü36), TCR $\alpha\beta$  (T10B9, BD Biosciences or IP26), and TCR $\gamma\delta$  (B1). Unless otherwise indicated, all antibodies were from Biolegend. Cells were washed in FACS buffer prior to acquisition on Fortessa or LSRII instruments (BD Biosciences) and analyzed with FlowJo. Gating strategies summarized in Supplementary Figure 13. Statistical tests were conducted using Prism (GraphPad version 8.0.2) with  $\alpha = 0.05$ .

## **Immunoblotting**

Cells were lysed in radioimmunoprecipitation assay buffer (RIPA buffer) supplemented with a protease and phosphatase inhibitor cocktail (Roche). Standard western blot procedures were followed. A rabbit monoclonal antibody against human MAGT1 (N-terminal sequence FINFPAKGKPKRGDTYELQVRGFS) was produced (Epitomics). The following antibodies were used to immunoprobe specific glycoproteins: anti-NKG2D (clone D-20, Santa Cruz), anti-CD70 (ab96323, Abcam), anti-CD28 (clone D2Z4E, Cell Signaling), anti- HLA-DR (clone TAL1B5, Abcam), anti-TCR- $\beta$  (clone H-197, Santa Cruz), anti-CERS2 (A303-193A, Bethyl Laboratories, Inc), anti-SLC4A7 (clone L-15, Santa Cruz), and anti-ICAM-3 (A304-334A, Bethyl). Anti- $\beta$ -tubulin antibody (clone AA2, Millipore Sigma), anti- $\beta$ -Actin (ab20272, Abcam), and anti-Hsp90 $\alpha\beta$  (clone 3H3C27, Biolegend) were used for loading control.

## **Determination of transferrin and apolipoprotein CIII (Apo-CIII) isoforms**

Transferrin and Apo-CIII isoforms in serum were identified by immunoaffinity liquid chromatography and electrospray mass spectrometry as previously described(46). In brief, 10  $\mu$ L of diluted sample were injected into a 200  $\mu$ L/minute flow of pH 7.4 phosphate buffer saline (PBS) and retained on an immuno-affinity column that is composed of 60% anti-human apolipoprotein CIII antibody and 40% anti-human transferrin antibody bound POROS® 20 AL media (Applied Biosystems). The immuno-affinity column is then washed for two minutes with PBS. Following the two-minute wash, captured proteins are eluted to a C4 column at 200  $\mu$ L/minute with pH 2.5, 100mM glycine and 2% acetic acid buffer. The C4 column is then washed with water/methanol/glacial acetic acid (97/2/1) to remove signal suppressing salts. The proteins are then eluted from the C4 column with methanol/water/glacial acetic acid/trifluoroacetic acid (94.5/5/0.5/0.04) and introduced into an API 4000 tandem mass spectrometer (MS) equipped with a Turbo V source configured for electrospray ionization. The MS is operated in positive Q1 scan mode with two scan ranges;  $m/z$  1090-2000 for Apo-CIII and  $m/z$  2000-3000 for transferrin.

## **Mass cytometry**

Cryopreserved PBMCs from 18 XMEN patients (A.1, A.2, A.3, D.1, E.1, G.1, G.2, H.1, I.2, J.1, J.2, K.1, K.2, L.1, L.2, N.1, P.1, and Q.1) , 11 ALPS patients, and 24 healthy volunteers were rapidly thawed at 37°C and washed in pre-warmed complete RPMI immediately prior to cell surface staining and acquisition. All reagents were from Fluidigm except where noted. Cells were first incubated with a 5 $\mu$ M solution of Cisplatin in PBS to mark dead cells. Cells were then washed and resuspended in Maxpar Cell Staining Buffer (MCSB). Human Fc-receptor blocking

solution (Biolegend) was added to each sample and incubated for 10 minutes at room temperature. All metal-labeled antibodies were purchased from Fluidigm. Biotin anti-human CD70 (Biolegend) was detected with Qdot-streptavidin conjugate (ThermoFisher). The antibody panel for deep immunophenotyping by CyTOF is summarized in Supplementary Table 7. Antibodies were diluted in MCSB at concentrations validated for minimal channel spill-over, added to each sample, and incubated for 30 minutes at room temperature. Cells were washed with MCSB two times. Cells were then fixed for 15min in a 1.6% solution of paraformaldehyde (Sigma) in PBS. Cell intercalation solution was prepared by adding Cell-ID Intercalator-Ir into Maxpar Fix and Perm Buffer to a final concentration of 125nM. Cells were incubated with cell intercalation solution overnight at 4°C. Cells were then washed once with MCSB and with Maxpar Water twice. Cells were finally resuspended in a water solution containing EQ Four Element Calibration Beads, immediately prior to CyTOF data acquisition at a cell concentration of  $10^6$  cells/mL and filtered into cell trainer cap tubes. Data were acquired on a Helios Mass Cytometer (Fluidigm) as previously described (47).

### **Computational methods and statistical analysis of Mass Cytometry data**

Raw mass cytometry data were normalized with the Normalizer algorithm as recommended by the software developers (48). Data were then analyzed using a pipeline custom-programmed in Python (Fast Density Clustering, available at [https://github.com/alexandreday/fast\\_density\\_clustering](https://github.com/alexandreday/fast_density_clustering)). Data were first gated as live singlet cells, using [EQ4<sup>-</sup>Cisplatin<sup>-</sup>] and [CD45<sup>+</sup>DNA(2n)] manual gates (Supplementary Figure 13D). Automatic identification of clusters of differentiation based on surface marker expression was performed using a new pipeline coined Hierarchical Agglomerative Learning (HAL-x)

(<https://pypi.org/project/hal-x>). In brief, HAL-x: 1) performs data clustering through a modified hierarchical agglomerative learning algorithm, 2) assigns a phenotype to each cluster across all models, 3) applies stochastic selection and random forest classification to identify defining features (e.g. frequencies or expression levels) for the cell clusters of each group of individuals (XMEN, ALPS or Healthy donor). This custom-programmed algorithm relies on cross-validated identification of high-density regions, followed by rapid random forest classification in the 32-dimensional space of surface markers. HAL-x then labeled all the cells in all samples (>15 million cells from 53 individuals) and computed the inverse hyperbolic sine and normalized frequencies for each leukocyte population. A random forest algorithm used the population frequencies to determine if samples were taken from XMEN, ALPS, or healthy tissues. A similar analysis was performed using the Python-based Phenograph application as previously described, for which a 1-million-cell downsampled subset of all the cells were randomly chosen across all samples for computation (31).

### **N-linked glycoproteome analysis**

Protein digestion, lectin enrichment and deglycosylation were performed as previously described(36, 49). In brief, following protein digestion, tryptic peptides were incubated for 60 minutes with a lectin mixture [Concanavalin A (Con A), Wheat germ agglutinin (WGA), and Ricinus Communis Agglutinin (RCA)] on filtration units. Due to the large size of the glycopeptide-lectin complexes, they were retained on the filter after washing away non-glycosylated peptides. This was followed by treating the samples with PNGase F in H<sub>2</sub><sup>18</sup>O, which leaves a characteristic mass shift on the previously glycosylated site. Deglycosylated peptides were then eluted and measured using LC-MS/MS analysis.

## LC-MS/MS analysis

Both enriched-deglycosylated peptides (glycoproteome analysis) and total proteome peptides were separated by a nanoflow High Performance Liquid Chromatography (HPLC) (Proxeon Biosystems, now Thermo Fisher Scientific) coupled to a Quadrupole-Orbitrap Mass Spectrometer (Q Exactive, Thermo Fisher Scientific) with a nanoelectrospray ion source (Proxeon Biosystems). MaxQuant software was used to analyze mass spectrometric raw data. We searched the MS/MS spectra against the Uniprot database by the Andromeda search engine incorporated in the MaxQuant framework. For the glycoproteome, Cysteine carbamidomethylation was set as a fixed modification and N-terminal acetylation, methionine oxidation and deamidation in H<sub>2</sub><sup>18</sup>O were set as variable modifications. For the proteome, Cysteine carbamidomethylation was set as a fixed modification. N-terminal acetylation and methionine oxidation were set as variable modifications. A false discovery rate (FDR) of 0.01 was required for proteins, peptides and sites. Enzyme specificity was set to trypsin allowing N-terminal cleavage to proline. A minimum of seven amino acids per identified peptide were required and two miscleavages were allowed. The initial allowed mass deviation of the precursor ion was up to 6 parts per million (ppm) and for the fragment masses it was up to 20 ppm. Mass accuracy of the precursor ions was improved by time-dependent recalibration algorithms of MaxQuant. The “match between runs” option was enabled to match identifications across different replicates. For both proteome and glycoproteome label-free quantification was performed by MaxQuant with standard settings. We analyzed the MaxQuant output data with the Perseus tools, which was also available in the MaxQuant environment.

## **Unsupervised hierarchical clustering and T-test analysis of glycoproteomics data**

A filter was initially applied to remove contaminants and anomalous data. A subsequent filter was then applied to identify canonical “class I” NxS/T sequons using a localization probability  $>0.75$  and a score difference  $>5$ . The values were then converted to a  $\log_2$  scale of intensity. The site table was then expanded, and a 50% valid value filter applied (which filtered for 9 valid values in total). Unsupervised hierarchical clustering (Euclidean distance) was then performed using automated data analysis tools, and the data presented as a heat map. A dendrogram was added to depict the relative similarity between samples. For subsequent identification of sites differently glycosylated/expressed between Group A and Group B, we set the FDR = 0.05 and  $S_0 = 0.25$ . The t-test values of the data were then presented as both a volcano plot (t-test difference vs.  $-\log$  t-test p-value) and as a heat map. The results of our mass spectrometry analysis have been deposited to the Mass Spectrometry Interactive Virtual Environment (MassIVE) datasets (<https://doi.org/doi:10.25345/C5MH21>).

## **Glycopeptide mapping**

Glycosites were categorized as previously described (19). In brief, the FASTA sequence for each significantly affected protein was downloaded from Uniprot (<https://www.uniprot.org/>). The affected glycosite was mapped onto the sequence, as were transmembrane (TM) domains predicted by the TMHMM Server v. 2.0 program (<http://www.cbs.dtu.dk/services/TMHMM/>). We categorized glycosites as follows: (C-term) within 55 amino acids of the C-terminus of the protein, (Near TM) within 60 amino acids of a predicted TM domain, (Loop) in short loops between TM domains, (Cys-Rich) in cysteine-rich domains of cysteine rich proteins, and/or (N-term) before the first TM domain of a multi-TM protein. Short loops were defined as less than

100 amino acids between the TM regions. Cysteine-rich proteins were defined as having greater than 4.0% cysteine as calculated by ExPASy's ProtParam tool

(<https://web.expasy.org/protparam/>). Glycosites in cysteine-rich proteins were defined as being in cysteine-rich domains if they fit at least one of the following criteria: (1) Either the +1 or +2 sites were a cysteine (ie. NCS/T or NXC), (2) there were at least 3 cysteines between the -9 and +10 positions surrounding the glycosite, or (3) the glycosite fell within a cysteine-rich domain predicted by ExPASy's PROSITE (<https://prosite.expasy.org/prosite.html>).

### **mRNA Electroporation.**

PBMCs were activated and cultured in complete medium with IL-2 for 2 weeks (described above). Then, cells were counted and resuspended in electroporation buffer (MaxCyte System) at  $2 \times 10^7$ /mL. RNA (100 $\mu$ g/mL) was added as indicated and electroporated per manufacture's specification. After electroporation, cells were incubated at 37°C for 20 min before transfer to complete medium for culture.

### **Statistics**

Unless otherwise stated, statistical analysis was conducted in GraphPad Prism (Version 8.1.2), *P*-values < 0.05 were considered statistically significant, and data are shown as the mean  $\pm$  the standard error of the mean. For multiple comparisons, ordinary one-way ANOVA with Tukey's multiple comparisons correction for all pairwise comparisons were used. To compare test samples relative to controls, the controls were normalized to 1 and a one sample t-test was conducted on the experimental samples with  $\mu = 1$ .

## **Study approval**

All subjects provided written informed consent for Institutional Review Board (IRB)-approved protocols at their respective institutions in accordance with the Declaration of Helsinki, and written informed consent was provided for pictures appearing in the manuscript.

## **Authorship Contributions**

J.C.R., M.M.L., G.A.B., and M.J.L. designed and supervised the research; J.C.R., S.P., K.B., A.P., D.K., H.M., P.A., C.T.V, J.F.R., J.O.A., S.G.H., N.C.P., and E.V. collected data; J.C.R., M.M.L., J.Z., M.B., S.J.D., P.J., A.M., G.N., G.A.B., B.S., L.Z., A.B.G., S.D.C., T.H., R.M., K.R., and S.S.D.R. performed research; J.C.R., M.M.L., J.Z., M.B., S.J.D., H.C.S., C.K., J.T.A., S.D.C., E.M., G.A.B., M.M., and M.J.L. analyzed and interpreted the data; St.P., A.P., and D.E.K. conducted pathology evaluations; J.C.R., M.M.L., S.J.D., S.D.C., S.H., and M.M. performed statistical analysis; A.G.R.D. and P.M. developed the data clustering algorithm, J.C.R., S.P., K.B., D.K., M.G., J.C., H.C.S., V.K.R., G.U., J.B., L.W., C.T., W.G., L.R.F., J.S.O., I.K.C., C.M.T.V., J.L.F., J.O.A., S.G.H., N.C.P., T.P., E.U., M.K., S.S.D.R., and H.L.M. provided clinical insight; J.C.R., M.M.L., M.J.L. and other authors wrote the manuscript; and all authors reviewed and edited the manuscript. J.C.R. and M.M.L. contributed equally to this work. J.C.R. led the clinical study and is in the first position of the author list.

## **Acknowledgments**

This work was supported by the Division of Intramural Research, NIAID, NIH; the Intramural Research Program of the National Human Genome Research Institute, NIH; the Japan Society for the Promotion of Science (JSPS) and NIH grant (71403), and by co-funding through the

Office of Disease Prevention, NIH. M.M.L was supported by Uehara Research Fellowship from Uehara Memorial Foundation (201330032). We also acknowledge the National Human Genome Research Institute and National Heart, Lung, and Blood Institute for their grant (UM1 HG006542) to the Baylor-Hopkins Center for Mendelian Genomics; NIAID for their grant (NIH R01-AI120989) to J.S.O; and COLCIENCIAS for their grant (1115-569-34430) to Universidad de Antioquia. This project has also been funded with federal funds from NCI, under Contract No. HHSN261200800001E. The content of this publication does not necessarily reflect the views or policies of the Department of Health and Human Services, nor does mention of trade names, commercial products, or organizations imply endorsement by the U.S. Government. The authors thank Ryan Kissinger for designing the diagrams, Brigit S. Sullivan for reviewing the manuscript; and Hudson H. Freeze for important insights and advice. We thank James R Lupski, Richard Gibbs and Zeynep Coban-Akdemir for their contribution in the genetic diagnosis of one of our patients. The CyTOF Facility at the Center for Human Immunology is supported by NIH intramural funding (AI001226-01). We thank Maxcyte Inc. for providing the MAGT1 and GFP mRNAs and their collaboration. Finally, we thank all patients described in this manuscript and their families for facilitating this work.

**Address correspondence to:** Michael J. Lenardo, Laboratory of Immune System Biology, NIAID, NIH, Building 10, Room 11N311, 10 Center Drive, MSC 1892, Bethesda, MD 20892-1892 USA. Phone 301-496-6754; Email: [lenardo@nih.gov](mailto:lenardo@nih.gov). Or to: Grégoire Altan-Bonnet, Center for Cancer Research, NCI, Building 37, Room 4134, Bethesda, MD 20892. Phone: 240-760-6888; Email: [gregoire.altan-bonnet@nih.gov](mailto:gregoire.altan-bonnet@nih.gov).

## **Disclosure of Conflicts of Interest**

The authors have declared that no conflict of interest exists.

## References

1. Li FY, Chaigne-Delalande B, Kanellopoulou C, Davis JC, Matthews HF, Douek DC, et al. Second messenger role for Mg<sup>2+</sup> revealed by human T-cell immunodeficiency. *Nature*. 2011;475(7357):471-6.
2. Chaigne-Delalande B, Li FY, O'Connor GM, Lukacs MJ, Jiang P, Zheng L, et al. Mg<sup>2+</sup> regulates cytotoxic functions of NK and CD8 T cells in chronic EBV infection through NKG2D. *Science*. 2013;341(6142):186-91.
3. Li FY, Chaigne-Delalande B, Su H, Uzel G, Matthews H, and Lenardo MJ. XMEN disease: a new primary immunodeficiency affecting Mg<sup>2+</sup> regulation of immunity against Epstein-Barr virus. *Blood*. 2014;123(14):2148-52.
4. Ravell J, Chaigne-Delalande B, and Lenardo M. X-linked immunodeficiency with magnesium defect, Epstein-Barr virus infection, and neoplasia disease: a combined immune deficiency with magnesium defect. *Curr Opin Pediatr*. 2014;26(6):713-9.
5. Fisher GH, Rosenberg FJ, Straus SE, Dale JK, Middleton LA, Lin AY, et al. Dominant interfering Fas gene mutations impair apoptosis in a human autoimmune lymphoproliferative syndrome. *Cell*. 1995;81(6):935-46.
6. Rieux-Laucat F, Le Deist F, Hivroz C, Roberts IA, Debatin KM, Fischer A, et al. Mutations in Fas associated with human lymphoproliferative syndrome and autoimmunity. *Science*. 1995;268(5215):1347-9.
7. Sneller MC, Straus SE, Jaffe ES, Jaffe JS, Fleisher TA, Stetler-Stevenson M, et al. A novel lymphoproliferative/autoimmune syndrome resembling murine *lpr/gld* disease. *J Clin Invest*. 1992;90(2):334-41.
8. Straus SE, Sneller M, Lenardo MJ, Puck JM, and Strober W. An inherited disorder of lymphocyte apoptosis: the autoimmune lymphoproliferative syndrome. *Ann Intern Med*. 1999;130(7):591-601.
9. Price S, Shaw PA, Seitz A, Joshi G, Davis J, Niemela JE, et al. Natural history of autoimmune lymphoproliferative syndrome associated with FAS gene mutations. *Blood*. 2014;123(13):1989-99.
10. Patiroglu T, Haluk Akar H, Gilmour K, Unal E, Akif Ozdemir M, Bibi S, et al. A case of XMEN syndrome presented with severe auto-immune disorders mimicking autoimmune lymphoproliferative disease. *Clin Immunol*. 2015;159(1):58-62.
11. Bleesing JJ, Brown MR, Dale JK, Straus SE, Lenardo MJ, Puck JM, et al. TcR-alpha/beta(+) CD4(-)CD8(-) T cells in humans with the autoimmune lymphoproliferative syndrome express a novel CD45 isoform that is analogous to murine B220 and represents a marker of altered O-glycan biosynthesis. *Clin Immunol*. 2001;100(3):314-24.
12. Lee HS, Qi Y, and Im W. Effects of N-glycosylation on protein conformation and dynamics: Protein Data Bank analysis and molecular dynamics simulation study. *Sci Rep*. 2015;5:8926.
13. Zhou H, and Clapham DE. Mammalian MagT1 and TUSC3 are required for cellular magnesium uptake and vertebrate embryonic development. *Proc Natl Acad Sci U S A*. 2009;106(37):15750-5.

14. Mohorko E, Owen RL, Malojcic G, Brozzo MS, Aebi M, and Glockshuber R. Structural basis of substrate specificity of human oligosaccharyl transferase subunit N33/Tusc3 and its role in regulating protein N-glycosylation. *Structure*. 2014;22(4):590-601.
15. Matsuda-Lennikov M, Biancalana M, Zou J, Ravell JC, Zheng L, Kanellopoulou C, et al. Magnesium transporter 1 (MAGT1) deficiency causes selective defects in N-linked glycosylation and expression of immune-response genes. *J Biol Chem*. 2019.
16. Kelleher DJ, and Gilmore R. An evolving view of the eukaryotic oligosaccharyltransferase. *Glycobiology*. 2006;16(4):47R-62R.
17. Ruiz-Canada C, Kelleher DJ, and Gilmore R. Cotranslational and posttranslational N-glycosylation of polypeptides by distinct mammalian OST isoforms. *Cell*. 2009;136(2):272-83.
18. Shrimal S, Trueman SF, and Gilmore R. Extreme C-terminal sites are posttranslocationally glycosylated by the STT3B isoform of the OST. *J Cell Biol*. 2013;201(1):81-95.
19. Cherepanova NA, Venev SV, Leszyk JD, Shaffer SA, and Gilmore R. Quantitative glycoproteomics reveals new classes of STT3A- and STT3B-dependent N-glycosylation sites. *J Cell Biol*. 2019;218(8):2782-96.
20. Cherepanova NA, Shrimal S, and Gilmore R. Oxidoreductase activity is necessary for N-glycosylation of cysteine-proximal acceptor sites in glycoproteins. *J Cell Biol*. 2014;206(4):525-39.
21. Freeze HH. Congenital Disorders of Glycosylation: CDG-I, CDG-II, and beyond. *Curr Mol Med*. 2007;7(4):389-96.
22. Jaeken J, and Matthijs G. Congenital disorders of glycosylation: a rapidly expanding disease family. *Annu Rev Genomics Hum Genet*. 2007;8:261-78.
23. Blommaert E, Peanne R, Cherepanova NA, Rymen D, Staels F, Jaeken J, et al. Mutations in MAGT1 lead to a glycosylation disorder with a variable phenotype. *Proc Natl Acad Sci U S A*. 2019;116(20):9865-70.
24. Dhalla F, Murray S, Sadler R, Chaigne-Delalande B, Sadaoka T, Soilleux E, et al. Identification of a novel mutation in MAGT1 and progressive multifocal leucoencephalopathy in a 58-year-old man with XMEN disease. *J Clin Immunol*. 2015;35(2):112-8.
25. Brigida I, Chiriaco M, Di Cesare S, Cittaro D, Di Matteo G, Giannelli S, et al. Large Deletion of MAGT1 Gene in a Patient with Classic Kaposi Sarcoma, CD4 Lymphopenia, and EBV Infection. *J Clin Immunol*. 2017;37(1):32-5.
26. He TY, Xia Y, Li CG, Li CR, Qi ZX, and Yang J. [X-linked immunodeficiency with magnesium defect, Epstein-Barr virus infection, and neoplasia: report of a family and literature review]. *Zhonghua Er Ke Za Zhi*. 2018;56(1):48-52.
27. Coffman RL, and Weissman IL. B220: a B cell-specific member of the T200 glycoprotein family. *Nature*. 1981;289(5799):681-3.
28. Zheng L, Li J, and Lenardo M. Restimulation-induced cell death: new medical and research perspectives. *Immunol Rev*. 2017;277(1):44-60.
29. van der Maaten L, and Hinton G. Visualizing Data using t-SNE. *J Mach Learn Res*. 2008;9:2579-605.

30. Mehta P, Bukov M, Wang C-H, Day AGR, Richardson C, Fisher CK, et al. *ArXiv e-prints*. 2018.
31. Levine JH, Simonds EF, Bendall SC, Davis KL, Amir el AD, Tadmor MD, et al. Data-Driven Phenotypic Dissection of AML Reveals Progenitor-like Cells that Correlate with Prognosis. *Cell*. 2015;162(1):184-97.
32. Wild R, Kowal J, Eyring J, Ngwa EM, Aebi M, and Locher KP. Structure of the yeast oligosaccharyltransferase complex gives insight into eukaryotic N-glycosylation. *Science*. 2018;359(6375):545-50.
33. Lanier LL. DAP10- and DAP12-associated receptors in innate immunity. *Immunol Rev*. 2009;227(1):150-60.
34. Karimi M, Cao TM, Baker JA, Verneris MR, Soares L, and Negrin RS. Silencing human NKG2D, DAP10, and DAP12 reduces cytotoxicity of activated CD8+ T cells and NK cells. *J Immunol*. 2005;175(12):7819-28.
35. Ho EL, Heusel JW, Brown MG, Matsumoto K, Scalzo AA, and Yokoyama WM. Murine Nkg2d and Cd94 are clustered within the natural killer complex and are expressed independently in natural killer cells. *Proc Natl Acad Sci U S A*. 1998;95(11):6320-5.
36. Zielinska DF, Gnad F, Wisniewski JR, and Mann M. Precision mapping of an in vivo N-glycoproteome reveals rigid topological and sequence constraints. *Cell*. 2010;141(5):897-907.
37. Schulz BL, Stirnimann CU, Grimshaw JP, Brozzo MS, Fritsch F, Mohorko E, et al. Oxidoreductase activity of oligosaccharyltransferase subunits Ost3p and Ost6p defines site-specific glycosylation efficiency. *Proc Natl Acad Sci U S A*. 2009;106(27):11061-6.
38. Jamaluddin MF, Bailey UM, and Schulz BL. Oligosaccharyltransferase subunits bind polypeptide substrate to locally enhance N-glycosylation. *Mol Cell Proteomics*. 2014;13(12):3286-93.
39. Karaoglu D, Kelleher DJ, and Gilmore R. Functional characterization of Ost3p. Loss of the 34-kD subunit of the *Saccharomyces cerevisiae* oligosaccharyltransferase results in biased underglycosylation of acceptor substrates. *J Cell Biol*. 1995;130(3):567-77.
40. Vaith P, Assmann G, and Uhlenbruck G. Characterization of the oligosaccharide side chain of apolipoprotein C-III from human plasma very low density lipoproteins. *Biochim Biophys Acta*. 1978;541(2):234-40.
41. Al Teneiji A, Bruun TU, Sidky S, Cordeiro D, Cohn RD, Mendoza-Londono R, et al. Phenotypic and genotypic spectrum of congenital disorders of glycosylation type I and type II. *Mol Genet Metab*. 2017;120(3):235-42.
42. Shrimal S, Ng BG, Losfeld ME, Gilmore R, and Freeze HH. Mutations in STT3A and STT3B cause two congenital disorders of glycosylation. *Hum Mol Genet*. 2013;22(22):4638-45.
43. Abolhassani H, Edwards ES, Ikinogullari A, Jing H, Borte S, Buggert M, et al. Combined immunodeficiency and Epstein-Barr virus-induced B cell malignancy in humans with inherited CD70 deficiency. *J Exp Med*. 2017;214(1):91-106.
44. Caminha I, Fleisher TA, Hornung RL, Dale JK, Niemela JE, Price S, et al. Using biomarkers to predict the presence of FAS mutations in patients with features of the autoimmune lymphoproliferative syndrome. *J Allergy Clin Immunol*. 2010;125(4):946-9 e6.
45. Pinheiro J, and Bates D. *Mixed-Effects Models in S and S-PLUS*. New York: Springer-Verlag New York; 2000.

46. Lacey JM, Bergen HR, Magera MJ, Naylor S, and O'Brien JF. Rapid determination of transferrin isoforms by immunoaffinity liquid chromatography and electrospray mass spectrometry. *Clin Chem*. 2001;47(3):513-8.
47. Bendall SC, Simonds EF, Qiu P, Amir el AD, Krutzik PO, Finck R, et al. Single-cell mass cytometry of differential immune and drug responses across a human hematopoietic continuum. *Science*. 2011;332(6030):687-96.
48. Finck R, Simonds EF, Jager A, Krishnaswamy S, Sachs K, Fantl W, et al. Normalization of mass cytometry data with bead standards. *Cytometry A*. 2013;83(5):483-94.
49. Deeb SJ, Cox J, Schmidt-Supprian M, and Mann M. N-linked glycosylation enrichment for in-depth cell surface proteomics of diffuse large B-cell lymphoma subtypes. *Mol Cell Proteomics*. 2014;13(1):240-51.

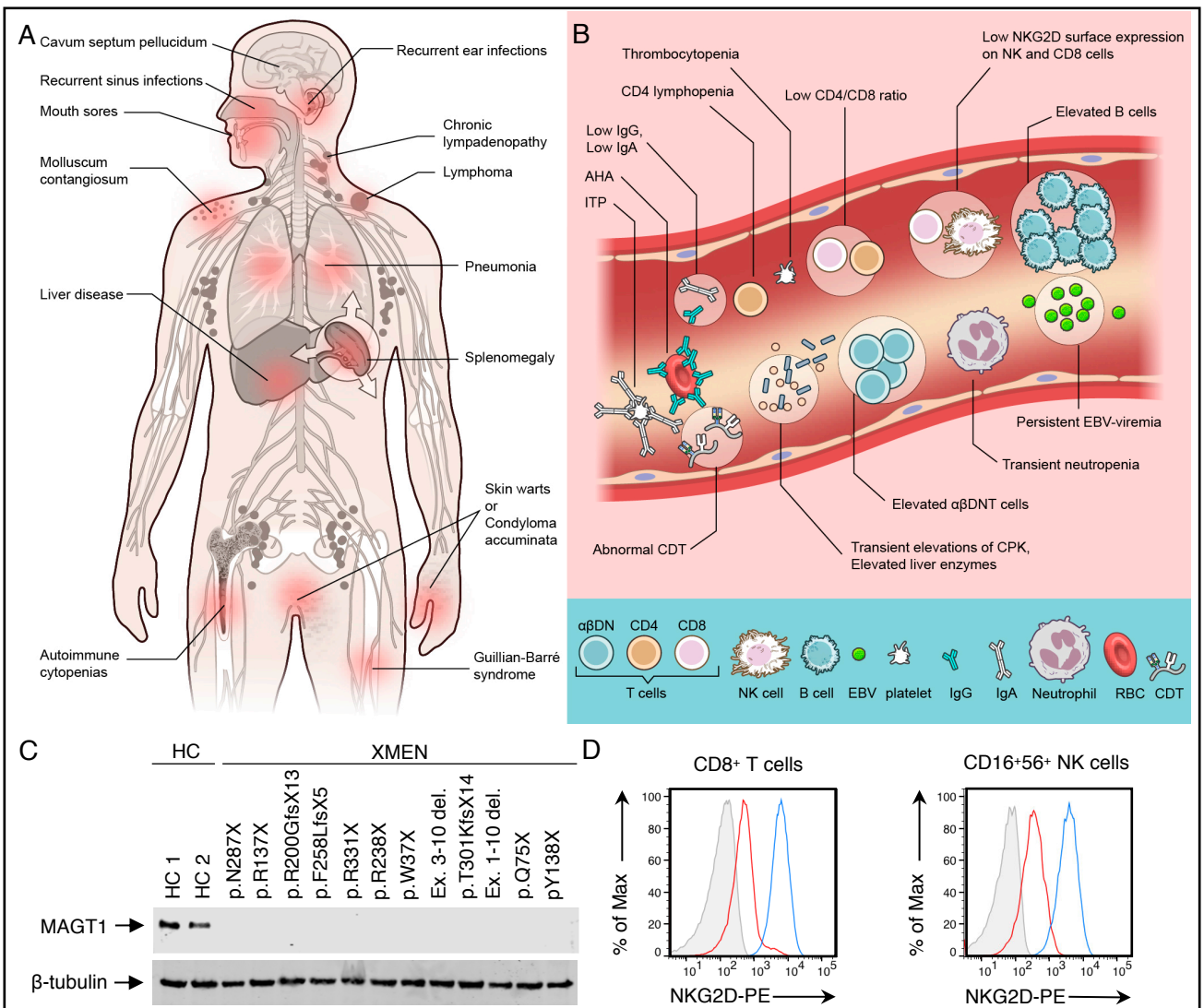


**Figure 1: Clinical, laboratory, and genetic findings in XMEN disease.** Clinical manifestations (A) and laboratory findings (B) in XMEN disease. Autoimmune hemolytic anemia (AHA), Immune thrombocytopenic purpura (ITP), Epstein-Barr virus (EBV), Carbohydrate Deficient Transferrin (CDT), alpha-beta double negative T cells ( $\alpha\beta$ DNT), creatine phosphokinase (CPK), and red blood cell (RBC). (C) Immunoblot showing MAGT1 and  $\beta$ -tubulin proteins in T cell blasts from healthy controls (HC1, HC2), and XMEN patients with indicated mutations. (D) NKG2D expression on CD8<sup>+</sup> T cells (left) and NK cells (right) from HC (blue) and XMEN patient (red) with isotype control (gray).

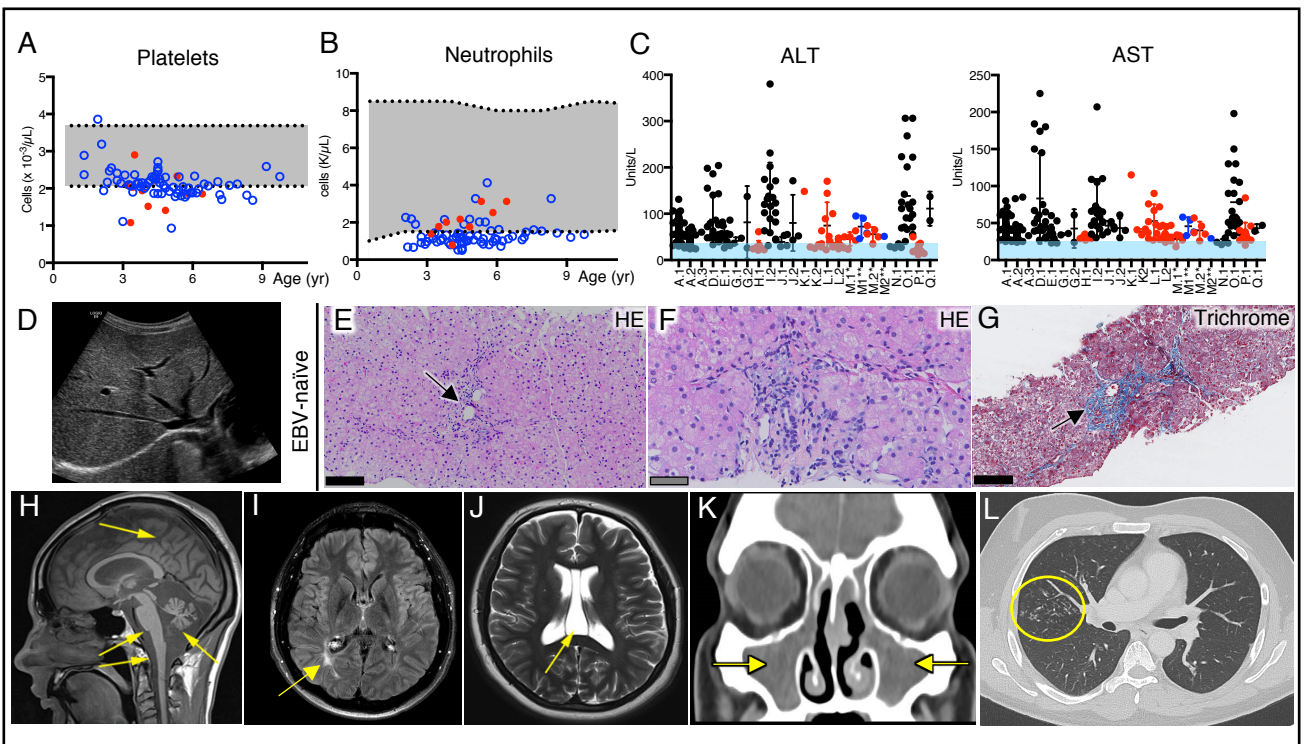


**Figure 2: Multisystem abnormalities in XMEN disease.** Platelet (A) and absolute neutrophil counts (B) for an EBV-naïve (red) and EBV-positive (blue) patient with normal range (gray) and patient's age in years (yr). (C) Levels of alanine aminotransferase (ALT) and aspartate aminotransferase (AST) in EBV-naïve (black), EBV-infected (red), and EBV-naïve patients who became EBV-infected (blue) with normal range (light blue) and patient identities on the x-axis. (D) Increased hepatic echogenicity in liver ultrasound from EBV-naïve patient. (E) and (F) Hematoxylin and eosin-stained (HE) liver biopsy from EBV-naïve patient showing mild focal portal chronic inflammatory infiltrates (black arrow) without interface hepatitis, and hepatocytes with pale cytoplasm. (G) Masson's trichrome stain of liver biopsy from same EBV-naïve patient shows periportal fibrosis (black arrow). Scale bars: 50  $\mu\text{m}$  (gray) and 100  $\mu\text{m}$  (black). (H) T1-weighted MRI demonstrating severe diffuse atrophy of the cerebrum, cerebellum, brainstem, and spinal cord (yellow arrows). (I) T2 fluid-attenuated inversion recovery (FLAIR) brain MRI showing occipital leukomalacia (yellow arrow). (J) T2-weighted brain MRI demonstrating cavum septum pellucidum (yellow arrow). (K) CT scan of paranasal sinuses showing opacification of the maxillary sinuses (yellow arrows) in patient with bacterial sinusitis. (L) CT scan showing extensive tree-in-bud nodular infiltrates in the right lung (yellow circle) in patient with longstanding hypogammaglobulinemia.

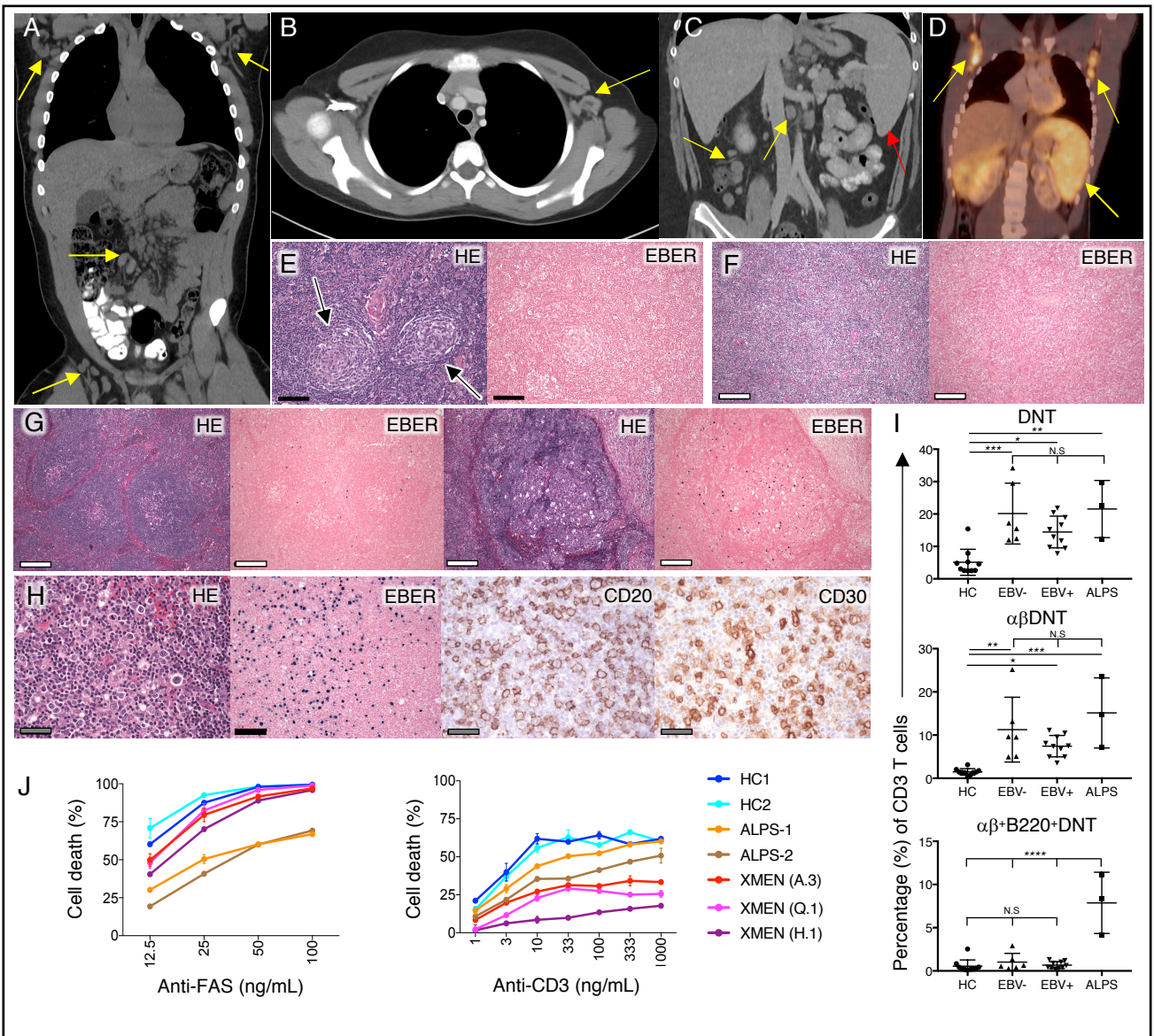


**Figure 3: Lymphoproliferation in XMEN disease.** (A) CT scan of chest, abdomen and pelvis depicting bilateral axillary, mesenteric, and inguinal lymphadenopathy (LAD) in an EBV-infected patient (yellow arrows). (B) Contrast-enhanced CT scan of the chest showing axillary LAD (yellow arrow) in an EBV-naïve patient. (C) Contrast-enhanced CT scan of the abdomen depicting splenomegaly (red arrow), and mesenteric LAD (yellow arrow) in an EBV-infected patient. (D) FDG-PET scan of XMEN patient with EBV-positive lymphoproliferative disease showing hypermetabolic splenomegaly and bilateral axillary LAD (yellow arrows). (E) HE stain of cervical lymph node (LN) biopsy from EBV-naïve patient showing reactive lymphoid hyperplasia with Castleman-like changes (black arrows) and negative EBV-encoded small RNAs (EBER) in situ hybridization staining. (F) Biopsy of large mediastinal mass showing lymphoid tissue obliterating normal LN architecture and negative EBER staining. (G) HE stained sections of an inguinal LN biopsy from EBV-positive patient showing reactive lymphoid hyperplasia and positive EBER stains. (H) HE, EBER, CD20, and CD30 staining of cervical LN biopsy from patient with EBV lymphoproliferative disease. Scale bars: 50  $\mu$ m (gray), 100  $\mu$ m (black) and 200  $\mu$ m (white). (I) Percentage relative to CD3<sup>+</sup> T cells of DNT,  $\alpha$  $\beta$ DNT, and B220<sup>+</sup> $\alpha$  $\beta$ DNT cells from age-matched healthy controls (HC, n=10), EBV-naïve (EBV-, n=6), EBV-infected (EBV+, n=10), and ALPS (n=3) patients. Data are expressed as mean  $\pm$  standard deviation. \* $P$  < 0.05, \*\* $P$  < 0.01, \*\*\* $P$  < 0.001, and \*\*\*\* $P$  < 0.0001 by ordinary one-way ANOVA with Tukey's multiple comparisons test ( $\alpha$  = 0.05). NS, not statistically significant. (J) Percentage of T cell death after treatment with different concentrations of agonistic anti-Fas antibody APO-1.3 (left) or anti-CD3 antibody (right) for healthy controls (HC), ALPS and XMEN (A.3, Q.1, and H.1) patients. Results are representative of all XMEN patients tested (n = 13) in three independent experiments.

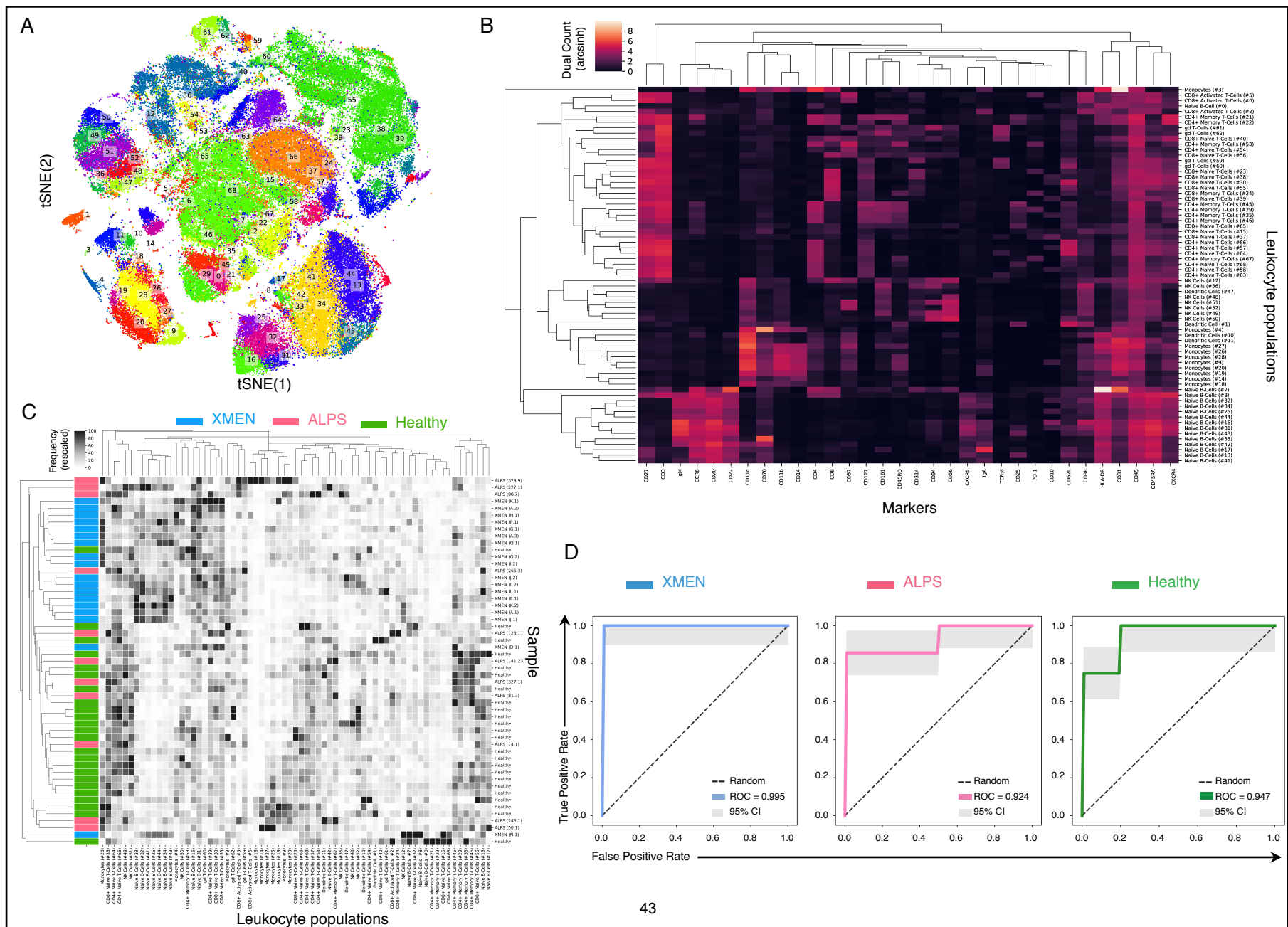
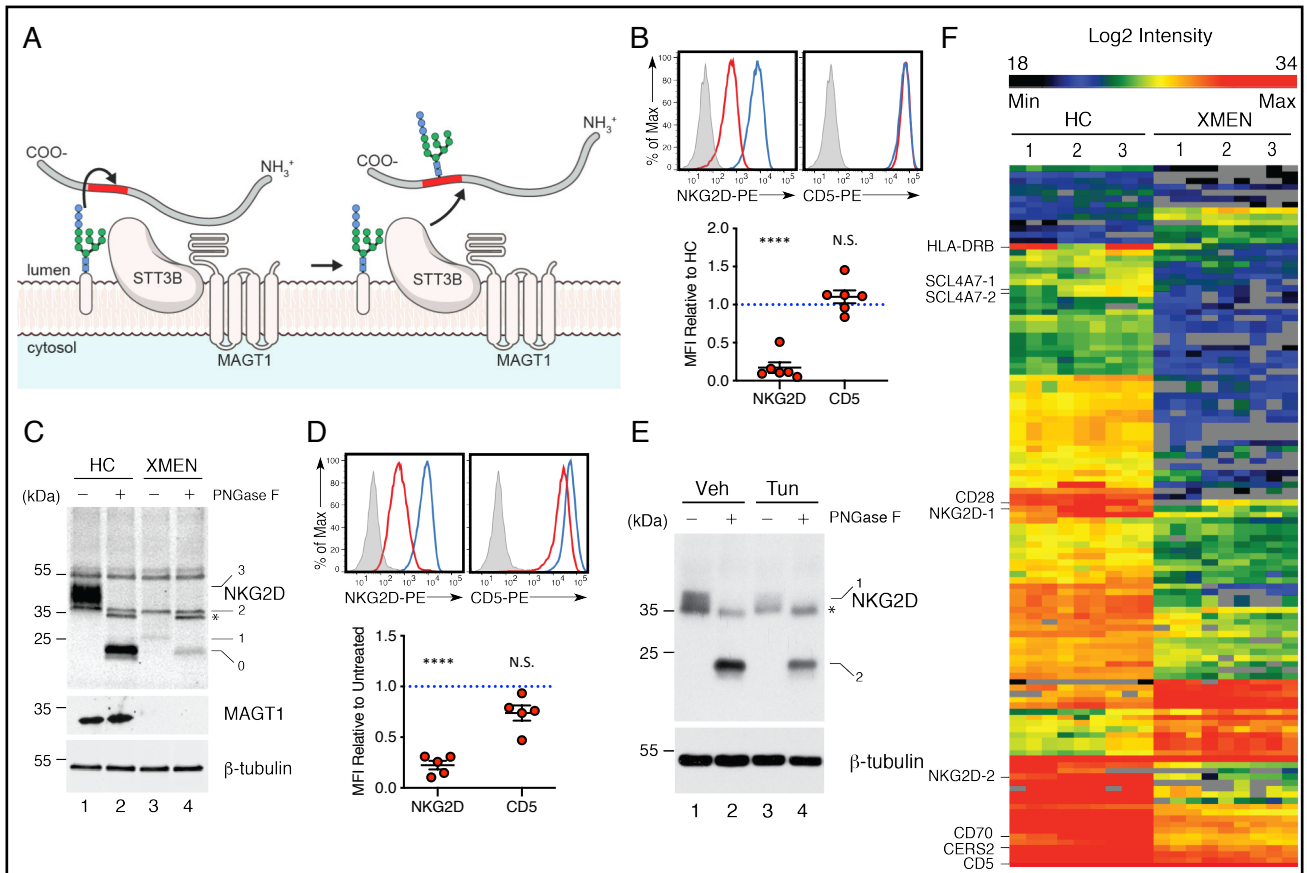
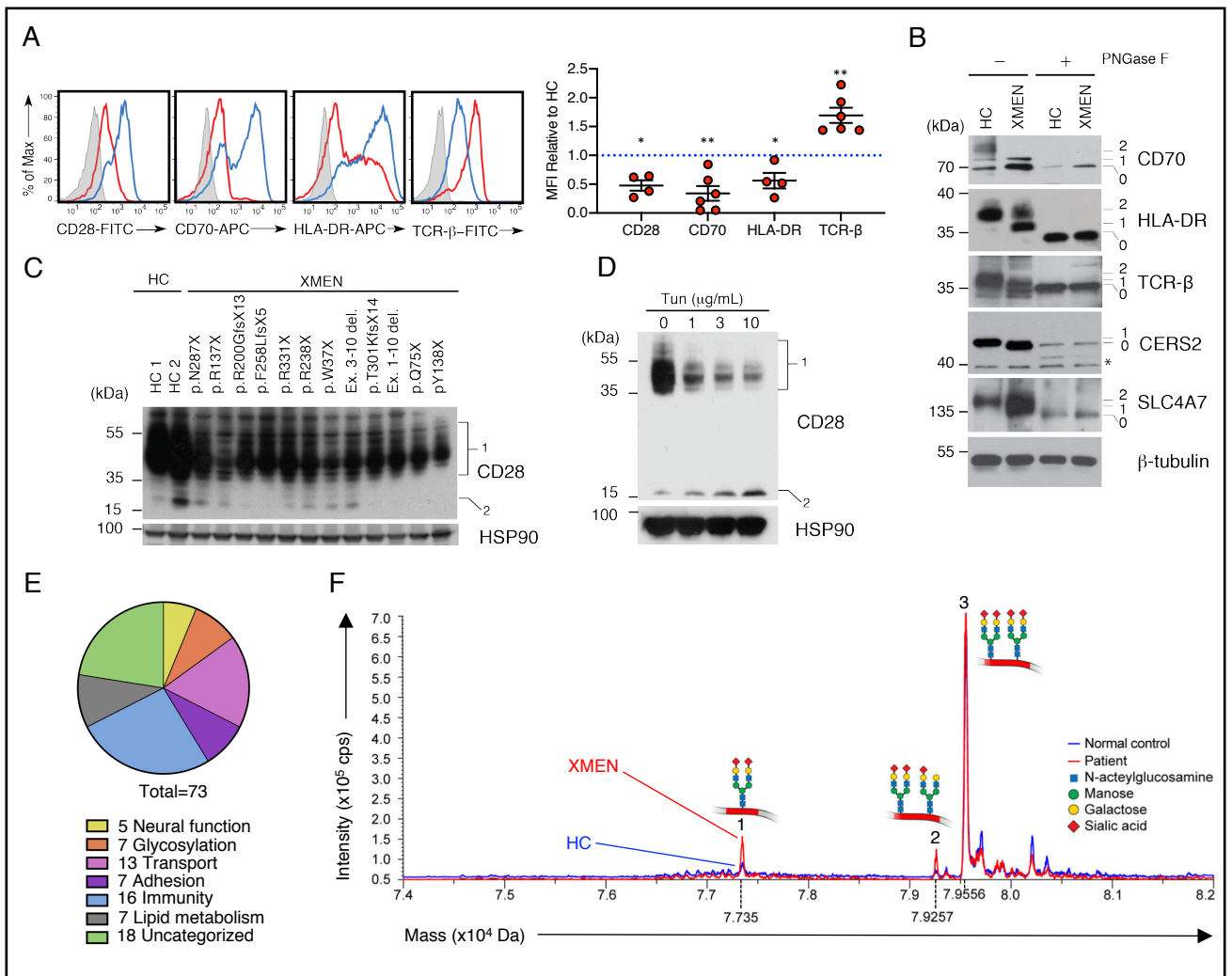


Figure 4

**Figure 4: Deep immunophenotyping of PBMCs shows distinctive immune subsets for XMEN compared to healthy controls and ALPS.** Hierarchical Agglomerative Learning (HAL-x) on CyTOF data acquired from PBMCs of XMEN (n=18), ALPS (n=11), and healthy controls (n=24) identifies 69 clusters of differentiation (CoD). (A) Two-dimensional projection of the identified CoD as visualized by t-SNE. (B) Dendrogram showing these CoD based on their abundance of surface epitopes. (C) Dendrogram for the frequencies of these CoD based on unsupervised grouping showing the clustering of XMEN patients (blue), ALPS patients (magenta), and healthy controls (green). (D) Receiver Operating Characteristic (ROC) for the random forest classification of XMEN, ALPS and healthy controls based on the frequency of their CoD. The area under the curve (AUC) value is the mean AUC taken after 4-fold cross-validation. Each fold of the cross-validation represents a different separation (of the patients) into training and testing sets. 95% confidence intervals (CI) are shown (gray).





**Figure 6: Impaired glycosylation of immune proteins and carbohydrate deficient transferrin pattern in XMEN disease (A)** Flow cytometry histogram (left) and MFI quantification relative to healthy controls (HC) (right) of CD28, CD70, HLA-DR, and TCR  $\beta$  in T cells from HC (blue) and XMEN (red) with unstained control (gray, n=6). (B) Immunoblot of CD70, HLA-DR, TCR- $\beta$ , CERS2, SLC4A7, and  $\beta$ -tubulin in T cells from HC and XMEN with (+) or without (-) PNGase F treatment. Unglycosylated (0), partially (1) and fully (2) glycosylated bands. (C) Immunoblotting of CD28 and HSP90 in T cells from HC (n=2) and XMEN (n=12) with indicated mutations. Glycosylated (1) and unglycosylated (2) CD28 bands. (D) Immunoblot blot of CD28 and HSP90 in T cells treated with DMSO (0) or tunicamycin (Tun) for 48 hours. Glycosylated (1) and unglycosylated (2) CD28 bands. Numbers on the left for immunoblots indicate kilodalton (kDa) standards. (E) Pie chart showing the biological function of abnormally glycosylated proteins in XMEN. (F) Mass spectrometry traces of a CDT test for HC (blue) and XMEN (red). Mass and intensity are expressed in Dalton (Da, X-axis) and counts per second (cps, Y-axis), respectively. Data are representative of five (B), two (C), and three (D) replicates. Mean  $\pm$  standard error of the mean. One-sample t-test with  $\mu=1$ . \* $P < 0.05$  and \*\* $P < 0.01$ . NS, not statistically significant.

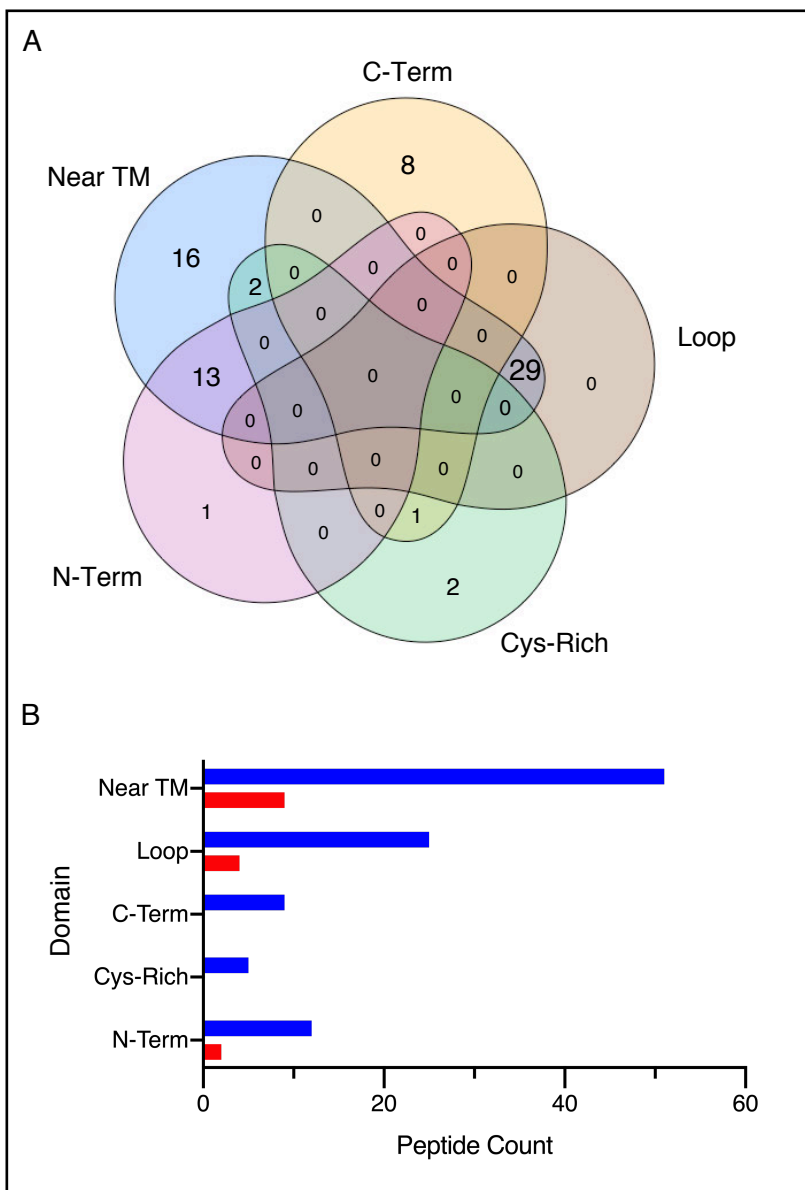


**Figure 7: Motifs of glycopeptides affected in XMEN disease. (A)** Venn diagram showing the number of differentially glycosylated peptides in XMEN that mapped to regions on a protein that were within the last 55 amino acids of the C-terminus (C-Term), in short loops between two transmembrane (TM) regions (Loop), in cysteine rich regions of cysteine-rich proteins (Cys-Rich), in the N-terminus domain of multi-TM proteins (N-Term), and/or were within 60 amino acids of TM regions. **(B)** Bar plot showing the counts of hypoglycosylated (blue) and hyperglycosylated (red) peptides in XMEN that mapped to the above regions.

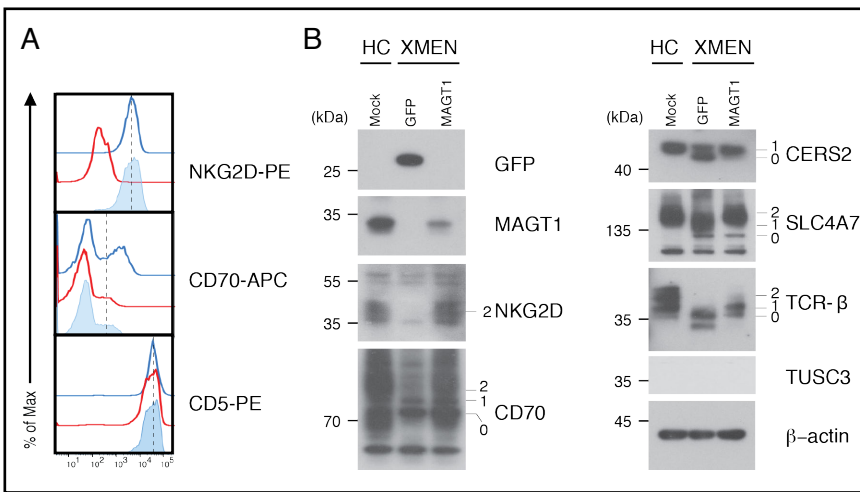


**Figure 8: Rescue of N-glycosylation by MAGT1 messenger RNA (mRNA) transfection in XMEN T Cells.** **A**, Flow cytometry histograms of NKG2D, CD70, and CD5 in T cells from a healthy control (HC, blue line) and XMEN 48 hours after transfection of mRNA encoding GFP (red line) or MAGT1 (light blue fill). **B**, Immunoblot of NKG2D, CD70, CERS2, TCR-β, SLC4A7 and β-Actin in T cells from HC and XMEN 48 hours after GFP or MAGT1 mRNA transfection. Fully-glycosylated (2), partially-glycosylated (1), and unglycosylated (0) bands are indicated. Data in **(A)** and **(B)** are representative of three independent experiments.

**Table 1: Clinical and laboratory features of XMEN disease**

<b>Clinical manifestations</b>	<b>Frequency</b>
Recurrent ear and sinopulmonary infections	70% (16/23)
Chronic lymphadenopathy	65% (15/23)
Splenomegaly	39% (9/23)
Lymphoma/LPD	39% (9/23)
Molluscum contagiosum	35% (8/23)
Recurrent mouth sores	35% (8/23)
Severe autoimmune cytopenias (grade 4)	35% (8/23)
Skin warts or condylomata acuminata	30% (7/23)
Guillain-Barré syndrome	17% (4/23)
HSV infection	13% (3/23)
Other autoimmune	13% (3/23)
Pericardial and/or pulmonary effusions	9% (2/23)
EBV-negative malignancy	4% (1/23)
<b>Laboratory and imaging findings</b>	
Transient elevation of ALT and AST liver enzymes	100% (23/23) *
Low NKG2D surface expression on NK and CD8 T cells	100% (23/23)
Elevated B cells	95% (22/23)
Elevated $\alpha\beta$ DNT cells	95% (19/20)
Low IgA	78% (18/23)
Low CD4/CD8 ratio	78% (18/23)
Low IgG	74% (17/23)
Persistent EBV-viremia	74% (17/23)†
Thrombocytopenia	70% (16/23)
Transient neutropenia	61% (14/23)
Transient elevations of CPK	52% (11/21)
CD4 lymphopenia	43% (9/21)
Cavum septum pellucidum	50% (4/8)
Central nervous system abnormalities	17% (4/23)

\*One patient had elevated liver enzymes only once out of multiple determinations. † All EBV-infected patients had persistent EBV-viremia.